ABSTRACT

BRADLEY, Rex Woodall. Characterization and Reclamation of Machining Swarf Generated by Superabrasive Grinding of Ceramics. (Under the direction of J. Michael Rigsbee and Paul Becher.)

This work examined the particle size of machining swarf generated during superabrasive grinding of silicon carbide, tetragonal zirconia polycystal and alumina workpiece materials. Grinding trials were carried out at surface speeds of 9.35 m/s, 19.7 m/s, 28.0 m/s, 37.9 m/s and 48.7 m/s for 40/50 120, 220, 320, and 600 wheel grit number diamond abrasive wheels. Swarf particle distributions were determined by laser light scattering analysis and related to machining parameters.

Silicon carbide swarf examined show a tendency toward bimodal particle distributions at low surface speeds and low wheel grit designations, with increasing surface speeds and higher wheel grit designations resulting in finer mean particle sizes due to a shift of particles from the coarse to the finer peak. Mean particle size trends correlated linearly with both surface speed and the abrasive particle size in the grinding wheel ranging from 3.36μm at 9.34 m/s using a 40/50 grit number wheel to 0.67μm at 48.7 m/s using a 600 grit number wheel.

Grinding of the tetragonal zirconia polycrystal material using a 600 grit number wheel at a surface speed of 48.7 m/s generated a mean particle size of 1.18μm. Observation of the tetragonal zirconia polycrystal swarf by SEM showed definite indications of plastic deformation based on the similarity of its chips with machining chips of ductile materials. Increased plasticity during abrasive interactions with the workpiece is believed to be the cause of the increase in mean particle size relative to silicon carbide swarf ground using identical machining parameters

Industrially generated alumina grinding waste was also characterized and analyzed to determine the potential for reclamation and reuse. The grinding swarf displayed a particle distribution with a mean particle size of 1.15μm. This powder was cleaned, pressed into a pellet and then sintered at 1500 $^{\circ}C$, with two other pellets hot pressed at a temperature of 1500 $^{\circ}C$ and 1600 $^{\circ}C$ at a pressure of 40ksi. These sintering trials resulted in a range of densities from 81.1% and 93.7% of the theoretical density of alumina.

Characterization and Reclamation of Machining Swarf Generated by Superabrasive Grinding of Ceramics

by
Rex Bradley

A thesis submitted to the Graduate Faculty of
North Carolina State University
In partial fulfillment of the
Requirements for the degree of
Master of Science

Materials Science and Engineering

Raleigh, NC

August 13th 2009

APPROVED BY:

_____	_____
Thomas A. Dow	Ronald O. Scattergood

_____
J. Michael Rigsbee
Committee Chair

BIOGRAPHY

REX W. BRADLEY was born in Fuquay-Varina, NC on August 12, 1981. He attended Harnett Central High School and graduated with Honors. In August of 2000 he began his study at North Carolina State University. In 2004 he graduated cum laude with a B.S. in Materials Science and Engineering and continued his pursuit of knowledge in the graduate school at North Carolina State University.

ACKNOWLEDGMENTS

I offer my thanks to my advisor Dr. J. M. Rigsbee who provided me the opportunity to continue my pursuit of knowledge and guided me along the way. I also would like to thank Dr. Paul Becher for his direction and advice throughout the course of this project. I extend my thanks to Dr. Matt Ferber, Dr. Ron Chand, Dr. Hong Wang and Dr. Andy Wereszczak for the guidance and input on this project, as well as their assistance in setting up the testing methodology. For setting up and carrying out the grinding trials examined during the course of this work I extend my thanks to Brian Jolly and Coury Fletcher. For their assistance in the area of materials characterization, I thank Shirley Waters and Dr. Fred Montgomery. I extend my thanks to Dr. Ron Scattergood and Dr. Tom Dow for serving as committee members on this work. I also thank Andy Newell for his aid throughout this project. I thank my family for their support throughout my pursuit of higher education. And lastly, for her enduring support, I offer special thanks to my wife Liz.

TABLE OF CONTENTS

LIST OF FIGURES

LIST OF TABLES

1 INTRODUCTION

The interaction of superabrasive grinding wheels with brittle materials leads to generation of workpiece particulate through fracture processes. This particulate, henceforth referred to as swarf, is swept away by the machining coolant flow and accumulates as waste in the collection tank within the coolant loop. This research effort characterized the particle size of the swarf generated by surface grinding of ceramic materials using a variety of wheel grits and grinding parameters. Through the study of these particles the following questions were answered.

- Can swarf material from ceramic grinding processes be reclaimed from the coolant fluid and reused to manufacture a sintered product?
- What relationships exist between machining parameters and particle sizes of ceramic machining swarf?
- Is surface grinding a feasible process for the generation of nanoscale ceramic particles?
- Can the swarf material be consolidated to useful densities using standard pressing and sintering processes?

2 BACKGROUND

This section will serve as a literature review providing a general overview of grinding material removal mechanics and the importance of abrasive processes in the machining of ceramics. Attention is given to the degree of brittle fracture and plasticity resulting from surface grinding of ceramics. The energetics at work during grinding and their relation to machining parameters are also covered in this section.

2.1 Overview of Surface Grinding

Abrasive processes have played a role in much of the technological development of humanity from its first use in tool production by early man to the precision lapping utilized by the microelectronics industry of today. [1] Grinding plays some role in nearly every product in use today, whether it be a direct role taken in machining the products themselves or an indirect role by machining of tools used to produce the products. [2] The ability of grinding processes to remove material by numerous small scale cutting operations allows for generation of favorable surface finishes and a high degree of demensional tolerance control in even brittle materials.

Typical grinding processes involve a randomly dispersed array of abrasive particles bound to a surface that is rotated at high speed while a workpiece is transversed across one of its faces. [3] The abrasive particles are of higher hardness than the workpiece material and fracture or cut its surface resulting in material removal. For materials with sufficient plasticity, or grinding conditions that allow for sufficient deformation, material removal can be thought of as numerous small scale machining events occurring, with each abrasive grain acting as a cutting surface producing fine machining chips.

Contact between the workpiece material and active cutting points in the grinding wheel occur most often at negative rake angles, meaning the angled face of the abrasive forms an angle of less than 90 degrees with respect to the workpiece surface. For the purposes of most grinding studies, the abrasive grains are assumed to be single cutting points, but in reality abrasive particles can have multiple cutting points that interact with the workpiece surface. [4] These cutting points are dynamic in nature and change as the

abrasives fragment and the bond material erodes. [5]

The interaction of the grinding wheel and workpiece surface during typical surface grinding is depicted below in Figure 2.1. The rotational velocity of the grinding wheel is denoted in this figure by V_w and the translational velocity of the workpiece is denoted by V_s. These parameters along with distance with which the workpiece is translated perpendicular to the width of the grinding wheel with each pass (crossfeed), the depth of cut and wheel grit comprise the variable machining parameters at the disposal of the machinist. Workpiece material is removed as it encounters the abrasive particles and the height of the surface is reduced by the thickness of the depth of cut as the workpiece is translated across the grinding wheel surface.

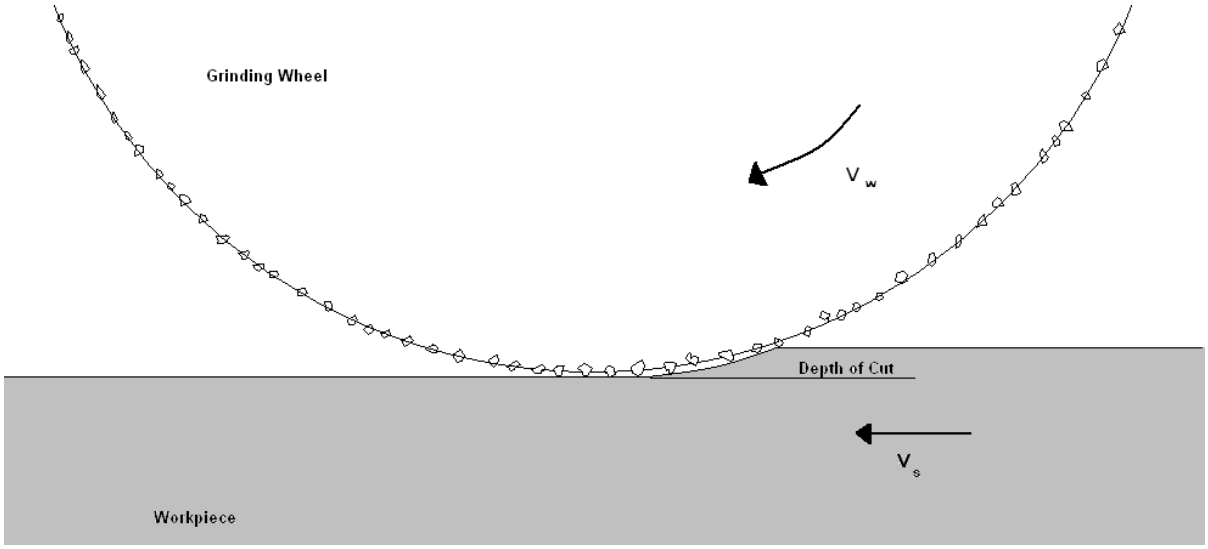

Figure 0.1 Depiction of the interaction between the grinding wheel and workpiece

2.2 Grinding of Ceramics

Ceramics present the potential for technological improvements in various applications due to their high temperature strength and stability. Forming ceramics into useful shapes presents unique challenges, due to their tendency to be hard and brittle most machining methods other than surface grinding are prohibited by high costs or excessive damage to the surface of the final part. Given the difficulty in sintering ceramics to the required dimensions and tolerances of a final product, machining is often a necessary step in the production of ceramic parts.

The cost of machining during the manufacturing process for ceramic parts in which a high degree of dimensional tolerance is required can range as high as 80% of the final part cost. [6] As such, the use of ceramics for many applications relies on maximizing the efficiency of the grinding process and optimization of the surface finish it produces. Surface damage induced by the grinding can significantly reduce the strength of a ceramic part unless the scale of the damage is reduced below the size of incipit flaws in the ceramic material. As such, ceramic grinding processes must often be carried out using conservative material removal rates or subsequent finishing must take place in order to remove grinding damage. With this in mind, numerous studies have attempted to determine material removal mechanisms during the grinding of ceramics as well as the optimal conditions for material removal while maintaining minimal surface damage. Generally these mechanisms are found to be coalescence of multiple cracks propagating normal to and perpendicular to the surface (median and lateral cracking) or along the grain boundaries.[7-9]

2.3 Brittle Fracture in Grinding of Ceramic Materials

Conventional grinding of ceramic materials is dominated by brittle fracture events as opposed to ductile chip formation in the grinding of metals. The high hardness of ceramic materials and correspondingly high yield strength result in greater difficulty in generating plastic deformation in comparison to metallic materials. [10] This disparity between ceramics and metals is displayed by the differences in hardness values shown below in table 2.1. The higher hardness values of ceramics shift the mechanisms of material removal for grinding processes to those dependant on brittle fracture events.

Table 2.1 Comparison of Vickers hardness values of various ceramics and metals [11-12]

Material	Vickers hardness, GPa
Al_2O_3	19.0-26.0
ZrO_2 (partially stabilized)	13.0
SiC	26.0-36.0
Ferrous Alloys	1.0-8.0
Aluminum Alloys	0.1-2.0

Similarities between fracture resulting from indentation and those resulting from grinding have led to the examining of material removal by sliding indentors as a model of a single interaction event between the workpiece material and an abrasive particle during grinding. [13] Due to very high localized stresses, indentation results in a region of deformation and microcracking directly under the indentation site. Beyond this contact

region a combination of median and lateral cracks extend and can facilitate material removal by their coalescence as shown in Figure 2.2. [14]

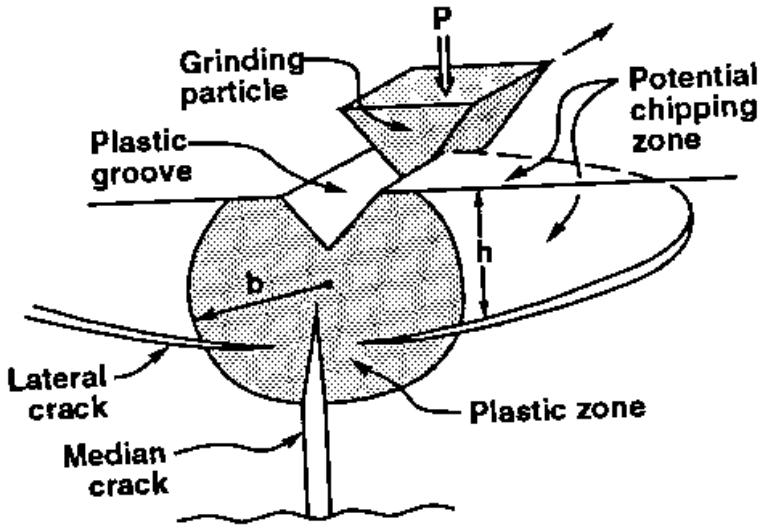

Figure 0.2 Interaction of a sliding indentor with a brittle material [14]

Damage from these sliding indentations bear a strong resemblance to the damage generated by static indentation. The stress fields associated with sliding contact differ from those of static ones in their asymmetric nature along the axis of translation. Single and multiple grit scratch experiments have been utilized to model the localized effects of abrasive particles during grinding causing extensive subsurface cracking on a polished ceramic surface. [15] The passing stress field occurring due to the moving indentor results in material removal by chipping as observed by the ejection of particles ahead of and behind the indentor under high speed photography. [16]

Brittle fracture of ceramics contributes to material removal during grinding in two ways, the coalescence of median and lateral cracks can chip away sections larger than the

grain size of the workpiece material or accumulation of microcracks can result in individual grain pullout. The relative influence of each on material removal during abrasive grinding of ceramics is dependant on the amount of force exerted per grit particle on the workpiece, with larger values favoring coalescence of median and lateral cracks.

Grain boundary strength of the workpiece materials has proven important in determining the dominant material removal mechanism during a given grinding process. The relative strength of a material's grain boundary relative to its lattice has an effect on whether cracks propagate inter- or trans-granularly. The effect of grain boundary strength is seen in homogenous equiaxed-grained silicon carbide as a more significant decrease in flexural strength following surface grinding as compared with heterogeneous silicon carbide comprised of elongated grains resulting from yttrium aluminum garnet addition. [17] In the case of these silicon carbides, the reduced grain boundary strength allowed for propogation of cracks along grain boundaries and reduced the size of cracks in the surface of the workpiece material to the order of the material's grain size.

When examining ground surfaces, the microcrack density is found to increase drastically in the near surface region relative to regions deeper below the machining surface. This has been termed pulverization and is believed to result from microcracking along cleavage planes resulting in the surface layer being densely populated by submicron particles, which are significantly finer than the material's grain size. [18] These particles appear to be loosely sintered by the temperatures associtaed with the grinding process. The thickness of this pulverization layer increases with brittleness of the workpiece and with the particle size of the diamond abrasive used in the grinding wheel. [18]

2.4 Plasticity in the Grinding of Ceramic Materials

Under the highly localized pressures and temperatures generated during grinding, even materials traditionally considered brittle have shown signs of plastic deformation. Direct observation of plastic deformation in the subsurface region of ground alumina has been possible utilizing transmission electron microscopy (TEM). Plasticity in alumina was observed as dense regions of dislocations or basal twinning in some grains with other grains appearing to lack plastic deformation. [19]

Plastic deformation during grinding of brittle materials is also apparent through the observation of dislocations in swarf particles. X-ray peak broadening grain size analysis of alumina grinding chips indicated a mean grain size of 30nm and a dislocation density of $2.75 \times 10^{11} cm^{-2}$. This study also indicated a mixture of finer particles significantly smaller than the workpiece grain size and coarser particles, on the scale of the work piece grain size appearing to occur from grain pullout.[20]

Ductile regime grinding seeks to prevent brittle fracture during the grinding of brittle materials through removal of material under conditions that promote plastic deformation and cutting. Figure 2.3 illustrates this process where chips are deformed from the material ultimately removing material with limited fracture. Such machining significantly improves surface finish, eliminating the necessity for further finishing processes, and improving the precision with which the workpiece can be machined. Ductile grinding theory states that during grinding the volume removed by plastic deformation (V_p) and that the area associated with brittle fracture (A_f) would relate to the depth of cut (a_e) as follows;

$$V_p \propto a_e^3$$

$$A_f \propto a_e^2$$

As the work of plastic deformation (E_p) is proportional to the volume of material deformed (V_p) and the energy involved in brittle fracture events (E_f) is proportional to area of fracture (A_f) the following relation is realized.

$$\frac{E_p}{E_f} \propto \frac{a_e^3}{a_e^2} \propto a_e$$

Thus, the ratio of energy associated with plastic deformation (E_p) and that of brittle fracture (E_f) are proportional to the depth of cut (a_e). Smaller depths of cut result in decreased strain rates, which favor plastic deformation and cutting as their primary material removal mechanism over removal by fracture. [21]

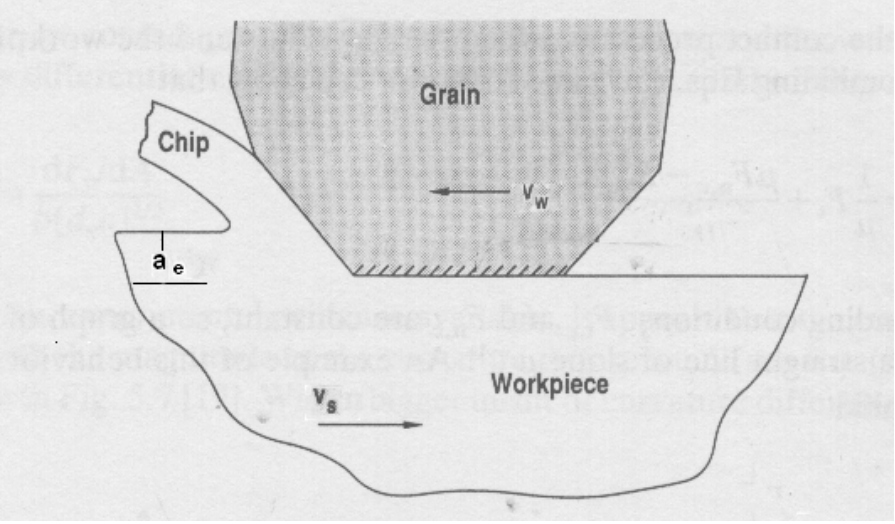

Figure 0.3 Material removal during grinding by ductile chip formation [2]

2.5 Maximum Undeformed Chip Thickness

Maximum undeformed chip thickness (h_{max}) can be determined by tracing the arc of a single abrasive grit as it cuts into the surface of the workpiece, as represented below in Figure 2.4. The h_{max} value for a grinding operation describes the maximum thickness of a machining chip assuming the chip is formed by cutting along the interaction line between an abrasive particle and the workpiece, assuming no distortion due to deformation. The geometry of this chip arises from the circular path of the abrasive particles bound to the outer edge of a rotating circular wheel.

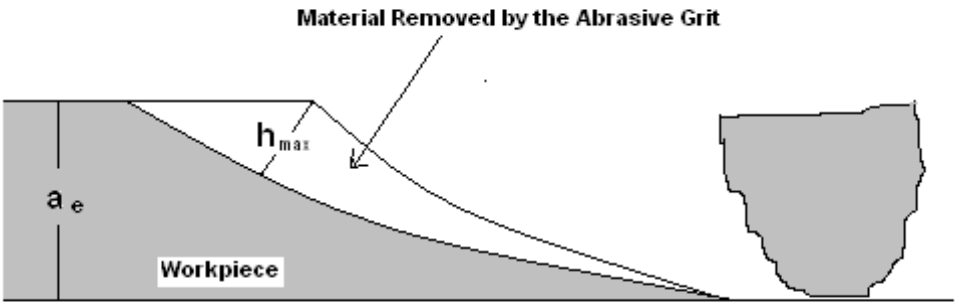

Figure 0.4 Depiction of the maximum undeformed chip thickness.

The value a_e in this figure is the depth of cut for the grinding operation. The maximum undeformed chip thickness (h_{max}) was proposed by Shaw, Reichenbach, and Mayer in the form seen in equation 2.1. [22]

$$h_{\max} = \left[\frac{4}{Cr} \left(\frac{v_w}{v_s} \right) \left(\frac{a_e}{d_s} \right)^{1/2} \right]^{1/2} \quad \textbf{(2.1)}$$

C is the density of cutting points

r is the ratio of chip width to average undeformed chip thickness

v_s is the surface speed of the wheel

v_w is the table speed

a_e is the depth of cut

d_s is the wheel diameter

The h_{max} parameter is an important characterizing value for grinding operations; also termed the grit depth of cut, it provides a numerical value for the depth with which abrasive grits attempt to cut into the workpiece during grinding. Larger values for the maximum grit depth of cut correspond to a more aggressive grinding operation with higher force per an abrasive particle values. Higher force per abrasive particle values tend to generate larger particles by fracture events, due to the increased tendency for material removal to occur by coalescence of lateral and median cracks. [10] The inverse relation between grind force and both wheel speed and number of cutting points is further supported by energy balance between the kinetic energy imparted by the grinding wheel and the strain energy absorbed by the machining chips [23]

2.6 Energy Considerations in the Grinding of Ceramics

Energy is transferred from the grinding wheel to the workpiece by several means include rubbing of the surface by the bond material in the wheel and cutting, plowing or fracture of the workpiece surface by the abrasive particles. This energy transfer is geometrically confined to the arc of contact between the grinding wheel and workpiece and as such can result in extensive heating of a localized area of the workpiece and subsequent surface damage. Determining the amount of energy required to remove a given volume of material gives the specific energy of the grinding operation. The specific energy (e_c) during a grinding operation is represented by equation 2.2. [24]:

$$e_c = \frac{F_t \cdot v_w}{a_p \cdot v_s \cdot a_e} \qquad \textbf{(2.2}$$

Where:

F_t is the tangential grinding force

v_w is the wheel speed

a_p is the grinding width

v_s is the workpiece speed

a_e is the depth of cut

Experimentally determined values for specific energy (e_c) during the grinding of ceramics typically range from 10^{11} to 10^{12} erg/cm^3. [25] These energy expenditure values are extraordinarily high and approach the theoretical shear strength of ceramic materials. Given the much lower energy levels required to remove material by brittle fracture, energy from the

grinding wheel must be utilized in ways other than merely the creation of new surface area through the generation of particles. This energy is dissipated in the form of heat, residual stresses in the chips and workpiece, plastic deformation and in the generation of new surface area. [26]

2.6.1 Effect of Grit Depth of Cut on Specific Energy (e_c)

Due to a phenomenon known as the "size effect", the specific energy (e_c) varies inversely with depth of cut rising significantly with decreasing average undeformed chip thickness. [27] The size effect is speculated to result from rounding of the abrasive particles on the grinding wheel. [28] The abrasive particle rounding results in less efficient cutting area and more plowing of the surface, where material is pushed aside by the passing abrasive without being removed, as the depth of cut is reduced. A similar change in specific energy is observed during transitions between machining modes. For example, a significant increase in specific energy is observed with the onset of ductile regime grinding, where material removal hinges on plastic deformation processes as opposed to fracture. [29]

2.6.2 Effect of Grain Size on Specific Energy (e_c)

A relation between specific energy (e_c) and the grain size of the workpiece also has been shown to exist, with finer grain sizes resulting in higher specific energies. [9] This relation is attributed to the relation between short crack toughness and grain size. Hence, coarser grained materials have less resistance to cracks on the scale of the materials grain

size, allowing for material removal by grain dislodgement to occur with lower specific energies in brittle materials comprised of coarser grains.

3 EXPERIMENTAL PROCEDURE

This section will serve to provide an overview of the materials and processes utilized to examine the relationships between grinding parameters and grinding swarf. Information is provided pertaining to the grinding machine and wheels as well as grinding parameters utilized during this research. Also included are the cleaning and consolidation techniques used to sinter grinding swarf obtained during this research.

3.1 Chemical Vapor Deposited Silicon Carbide

Grinding experiments were performed on a chemical vapor deposited silicon carbide material with a microstructure as seen below in Images 3.1a-b. The manufacturing process used to generate this material results in a combination of hexagonal alpha grains and face-centered cubic beta grains.[30] The microstructure of the material displays relatively large alpha silicon carbide grains used to seed the deposition process in order to lower the nucleation barrier, thus improving growth rates. The surrounding microstructure displayed significantly finer regions of alpha/beta silicon carbide nucleating from the seeding particles. Figure 3.1b shows a higher magnification view of several of the seeding particles. These particles are roughly 15 μm in diameter and are surrounded by alpha/beta regions, which nucleated and grew in a columnar fashion. Beyond the columnar nucleation regions a mixture of alpha and beta grains with an equiaxed structure that was submicron in size.

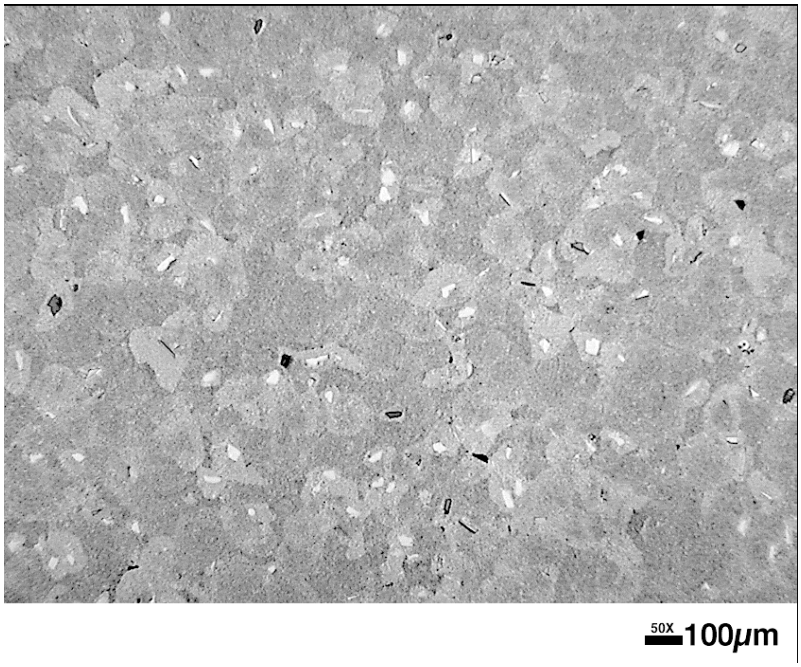

Figure 3.1a Optical micrograph of chemical vapor deposited silicon carbide

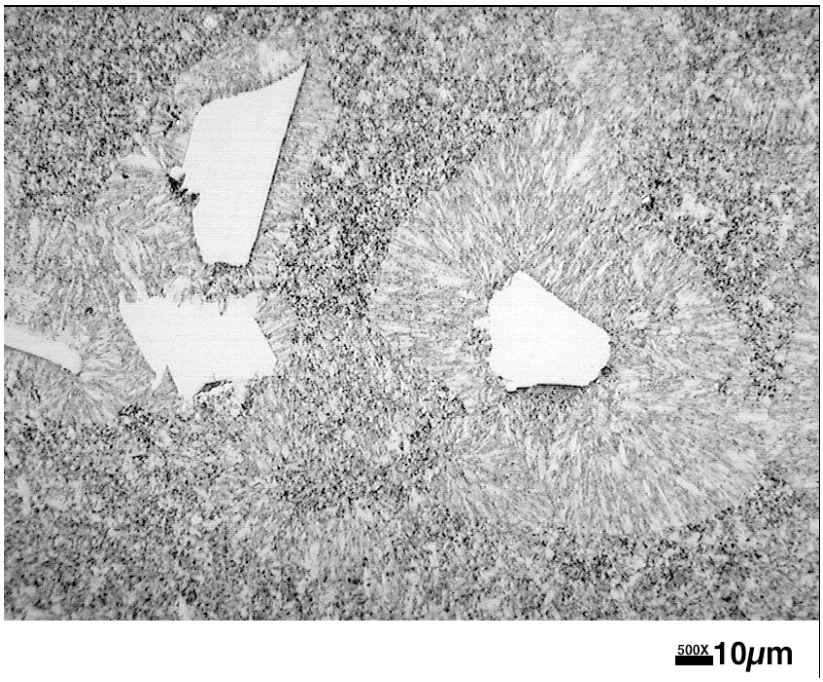

Figure 3.1b Optical micrograph showing the effects of seeding particles on silicon carbide growth during chemical vapor deposition

The silicon carbide material displays a Vickers hardness of 2850 kg/mm^2. The manufacturer reported a grain size of 5-10 microns, although some of the regions beyond the seeded nucleation sites appear significantly smaller. Image analyses of micrographs taken from polished samples of this material indicate the seeding material comprises approximately 10 vol. % of the ceramic sample. The material is reported to be 99.9% of the theoretical density of silicon carbide. [30]

3.2 Tetragonal Zirconia Polycrystal

Tetragonal zirconia polycrystal (TZP) is a polycrystalline zirconia that displays a uniform tetragonal microstructure at room temperature, as a result of the addition of 2.5 wt% yittria. The tetragonal crystals are metastable at low temperatures and transform to the equilibrium monoclinic crystal structure under applied stresses. This stress-induced phase transformation allows for significant transformation induced plasticity as the expanding tetragonal grains impose a compressive force on the propagating crack fronts. [31]
The TZP material was ground at a wheel speed of 46.7 m/s in order to examine the effect its finer grain size would have on the particle size distribution. This material's grain size distribution is display below in Figure 3.2.

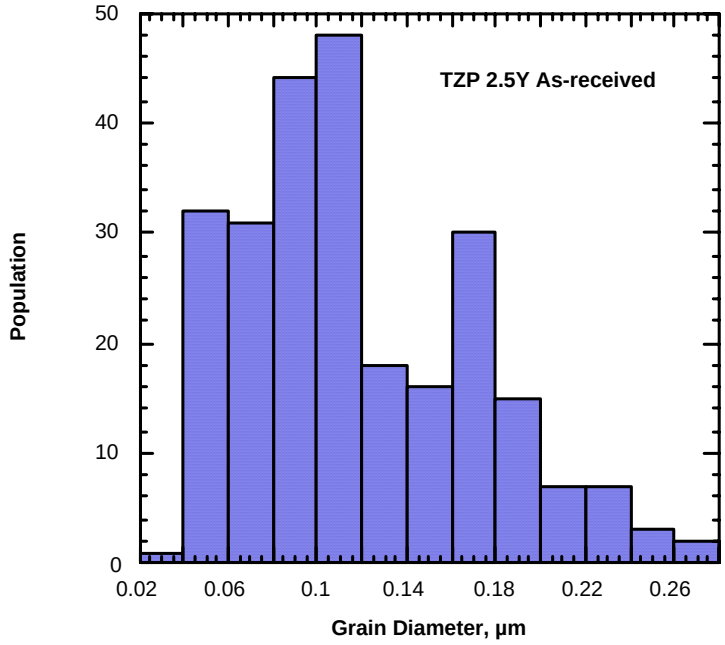

Figure 3.2 TZP Grain Size Distribution[1]

3.3 Coors AD-995 Alumina

AD-995 is a Coors designation for 99.5% pure alumina with a density of 3.9 gm/cm^3. The average grain size of the material is 6 micrometers and it has a Rockwell 45N hardness of 83 GPa. [32] The grinding swarf generated from this material was collected from coolant tanks in an industrial Blanchard grinding operation[2] and examined with regard to its particle size and potential for reclamation. This material and grinding process was selected as it provided a significant quantity of readily available swarf material, allowing for sintering studies to be preformed.

[1] Courtesy of Dr. Paul Becher Ph D. Oak Ridge National Laboratory
[2] Courtesy of T. Cornett, CoorsTek, Oak Ridge, TN

3.4 Grinding Wheels

Grinding wheels are commonly identified by the abrasive material they contain, the bond type used to contain the abrasive, and a grit number. This number increases as the size of the abrasive particles in the wheel decreases. Henceforth this number will be termed the wheel grit number to avoid confusion with size of the wheel's abrasive particles.

The Grinding wheels used for this study are listed below in Table 3.1 along with relevant information about each grinding wheel. Wheels utilized in this study were manufactured by Coors Tech, Norton, or Engis Corp. An approximate abrasive size based on the wheel grit numbers is also included for comparison purposes.

Table 3.1 Wheel grit number and abrasive size information for grinding wheels used in this study

Wheel Grit Number	Manufacturer	Wheel Designation	Bond Type	Wheel Size (in)	Approximate Abrasive Size (μm)
40/50	Engis Corp	HS 17769-1 D-40/50	Metal-Bonded	7	427
120	Norton	SD120R-100B99 1/8"	Resin-Bonded	7	150
220	Norton	SD220R-100B99 1/8"	Resin-Bonded	7	76
320	Coors Tech	DN320R-100B 1/8"	Resin-Bonded	6	54
600	Coors Tech	DN600R-100B 1/8"	Resin-Bonded	6	30

The resin-bonded wheels were dressed and trued with a rotary dresser. This process uses a rotating abrasive wheel mounted to the magnetic chuck of the grinding machining in order to minimize axial and radial runout, thus squaring the face of the grinding wheel in

reference to the chuck and grinding the wheel to a uniform diameter. The wheels were then hand honed by applying an alumina stick to the grinding face while the wheel rotates; this served to further expose the abrasive particles of the grinding wheel. Following these conditioning operations, the wheels were thoroughly flushed with tap water while spinning in an effort to remove loose particles generated during the dressing process. The Engris Corp wheel does not require dressing or truing as it is comprised of a single layer of diamonds attached to the metal hub by metallic plating.

3.5 Grinding Process and Collection

A Chevalier Smart Surface H-818 II surface grinder located in the High Temperature Materials Laboratory at Oak Ridge National Laboratory was utilized for all grinding trials during the course of this work. The silicon carbide workpiece was mounted in a vice attached to the grinder's magnetic chuck and the TZP workpiece, which was smaller in size, was attached via crystal bond to a metal plate that was in turn held by the vice. The vice and workpiece were surrounded by a containment vessel to facilitate isolation of the coolant and collection of the grinding swarf. Tap water was utilized as a coolant and was circulated using a submersible pump at a pumping speed of roughly 2 gallons per minute.

Surface grinding was conducted in climb mode, where the translation of the workpiece moves it into a clockwise rotating wheel, as shown in Figure 2.1. As indicated in Figure 2.4 the area of greatest interaction is near the original surface of the workpiece. Due to this fact the climb mode was chosen as swarf removed from the workpiece at the region of greatest interaction, between the grinding wheel and the surface is forced by the motion of

the grinding wheel along the machining interface. This allows for the swarf particles to be further reduced in size through continued interaction with the grinding wheel and the workpiece. Grinding was carried out for all trials according to the feed parameters shown below in Table 3.2. These feed parameters where arrived at by first attempting more aggressive rates to produce swarf material at a greater rate and then reducing the parameters to prevent chipping by fracture of the workpiece.

Table 3.2 Feed parameters utilized for grinding trials

Crossfeed	2.54mm
Total Crossfeed	50.8mm
Depth of Cut	0.00508mm
Total Downfeed	0.0254mm
Table Speed	5.6 m/min

Grinding was carried out at the surface speeds displayed in Table 3.3. These surface speeds correspond to 1000 rpm increments for the 7” diameter used in this work. The surface speeds where held constant for 6” diameter wheels by rotating them at higher rates. Surface speeds were limited at the high end due to the constraints placed on maximal forces in the wheel by its resin binding, which prevent wheel speeds higher than those used in this study. All surface speeds where calculated based rotations per a minute of the grinding wheels and their diameters.

Table 3.3 Wheel and surface speeds investigated during grinding trials

7” Wheel RPM	6” Wheel RPM	Grinding Surface Speeds (m/s)
1000	1167	9.3
2000	2334	19.7
3000	3500	28.0
4000	4667	37.4
5000	5833	46.7

The swarf material remained thoroughly dispersed in the coolant fluid due to the agitation provided by the movement of the workpiece table and to the circulation of the fluid by the coolant pump. Samples of the coolant containing swarf material generated by the grinding process were taken as the fluid continued to circulate through the coolant nozzle of the grinder following the completion of each grinding trial. The collection vat was cleaned between trials and wheels were flushed with water before beginning subsequent runs to remove chip material adhered to the grinding wheel.

3.6 Scanning Electron Microscopy

A Hitachi S4100 Field emission SEM located at Oak Ridge National Labs and a Hitachi 3200-N SEM located in the Analytical Instrument Facility at North Carolina State University were utilized to obtain information about the swarf particle size and morphology.

Suspensions of the grinding swarf were deposited on carbon tape, dried, and then coated with carbon to reduce the effects of charging during observation in the SEM. All images were obtained in the secondary electron mode at a beam voltage of 3 KeV, with EDS performed in some cases to verify that the observed particles came from the workpiece material.

3.7 Laser Light Scattering Particle Size Analysis

Particle Size Distributions were determined by utilizing a Horiba laser light scattering particle analyzer, LA-700. The device examines light scattering of a Helium-Neon laser by particles suspended in a fluid. This light scattering system detects particles between 0.04 and 262 micrometers using a combination of Fraunhofer diffraction and Mie scattering theory. [33] For all testing carried out in this work swarf samples were added to deionized water in concentrations adequate for the scattering information to be obtained.

The pH value of solutions containing the silicon carbide swarf samples were adjusted to 10.3 using ammonium hydroxide in order to aid in particle dispersion by electrostatic means. All the silicon carbide, zirconia, and alumina samples in this study showed finer distributions following ultrasonic dispersion for a period of 2 minutes by the LA-700 in addition to the agitation provided by its stirring apparatus to further reduce agglomeration. Attempts at using ultrasonic dispersion for periods beyond 2 minutes did not further deagglomerate the powder samples and for dispersion periods beyond 5 minutes the powders actually became more agglomerated.

3.8 Single-Grit Pendulum Scratch Test

The scratch hardness of the silicon carbide material was determined using a single-grit pendulum scratch hardness apparatus built at Michigan Technological University. These tests were carried out under the direction of Dr. Hong Wang at Oak Ridge National Labs. The scratch test device uses a pneumatic piston to drive a pendulum containing a conical diamond indentor along an arc into the surface of a polished test specimen. The forces normal and tangential to the scratch were measured by Kistler load cells. The force values are then passed through a charge amplifier, digitized and recorded using a lab view application at a sampling rate of 10^6 Hz. The cross-sectional area of material removed along the scratch was subsequently mapped by laser profilometry (Rodenstock RM-600, Munich, Germany) at Oak Ridge National Labs. The Rodenstock RM-600 laser profilometer has a resolution of 2 nm in the depth of the scratch. The spacing between measurements was 8 μm between scans across the width of the scratch with measurements taken every 0.4 μm along each scan. This allowed for calculation of the scratch hardness of the material and the specific energy of removal for the test scratch. [34]

Optical microscopy of the scratches was carried out using a Zeiss optical microscope and images were captured using an attached CCD camera. These images were used to examine the degree of cracking and chipping occurring at the workpiece surface due to the scratch testing as well as providing an image to compare with positions force data plots. They also provided insight into the relation between cracking and the recorded force plots.

3.9 Coors Alumina Swarf

The AD-995 alumina material was machined using Blanchard grinding and the resulting swarf was collected by sampling solids from the cutting fluid. This mixture of cutting fluid and alumina particles were heated in air in a convection oven at 350 $^{\circ}C$ for 8hrs to evaporate hydrocarbon corrosion inhibitors present in the coolant fluid, as observed by thermo gravimetric analysis (TGA) in Figure 3.3. The most prominent of the inverse peaks on the TGA scan at approximately 110 $^{\circ}C$ is due to residual water and the smaller inverse peaks at approximately 260 $^{\circ}C$ and 370 $^{\circ}C$ are attributed to evaporation of the corrosion inhibitors added to the fluid. The water inverse peak is shifted from 100 $^{\circ}C$ due to the lag time required to evaporate the fluid with respect to the heating rate.

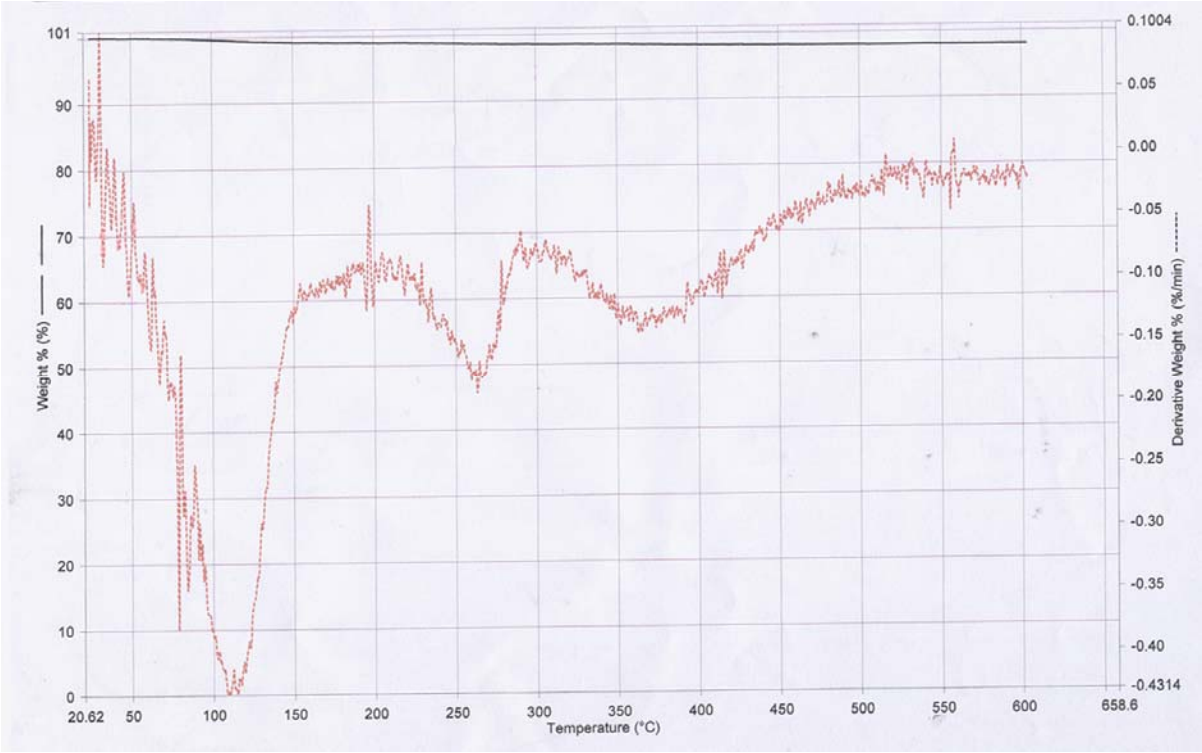

3.3 TGA scan of Coors alumina grinding swarf

After heating, the powder was subsequently washed in deionized water and electrostatically dispersed. Dispersion was carried out by adjusting the pH of deionized water containing the powder to 4.0 using hydrochloric acid. Particle size distributions were analyzed using the Horiba laser light scattering system. Attempts were also made at observing individual particles by scanning electron microscopy; however the material agglomerated readily, which prohibited observation of lone particles. The suspended powder was then dried, washed and mixed, by ball additive milling for 1 hour, with 1.5 wt% MgO from Alfa Asear to serve as a sintering aid. This powder was then sintered at 1500 $^{\circ}C$ after being cold pressed to a green pellet. A separate green pellet was hot pressed at a temperature of 1600 $^{\circ}C$ and a pressure of 40ksi.

4. 0 RESULTS

Presentation of results from this research will focus first on particle distributions from swarf generated during surface grinding of the silicon carbide material. Material removal mechanisms and energy considerations will then be examined with the single grit pendulum scratch test. Particle size distributions and SEM micrographs of swarf generated by grinding of TZP and alumina materials are subsequently presented. Finally, the results of reclamation efforts and sintering results for the alumina powder are presented.

4.1 Particle Size Distributions of Silicon Carbide Grinding Swarf

The particle size distributions of silicon carbide swarf generated at a series of wheel speeds are displayed Figures 3.1a-e for each grinding wheel. Data is presented as the fractional percent of the distribution (F%) at a given particle size. Particle distributions are count-based as opposed to distributions formed on a volume faction basis. This results in an apparent larger fraction of fine particles than would be observed through methods which determine particle distributions on a volume basis.

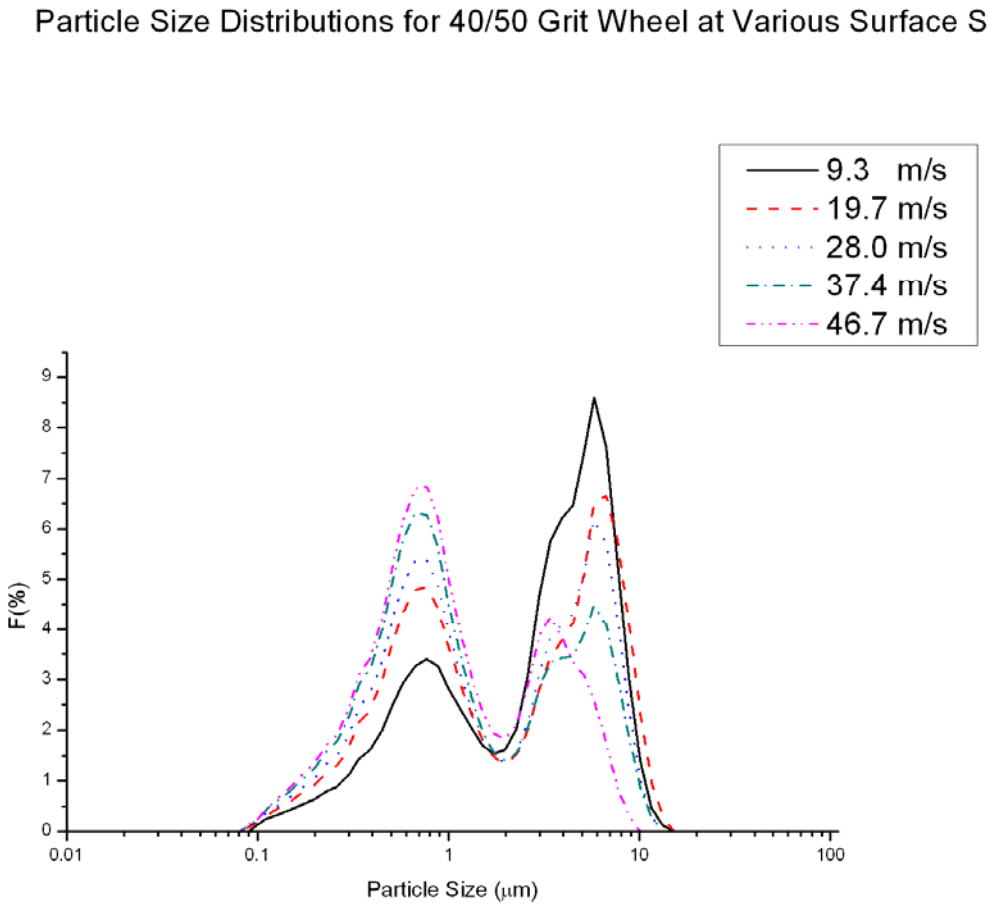

Figure 4.1a Particle size distributions obtained for the 40/50 wheel grit number

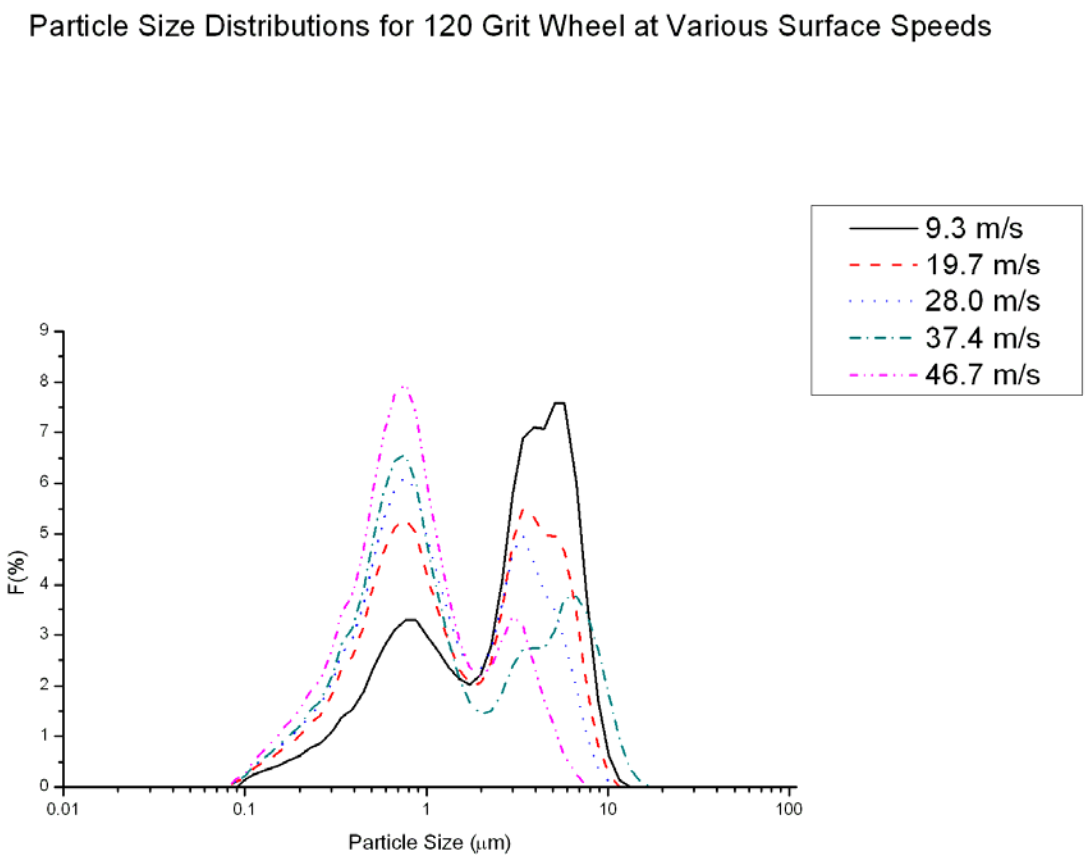

Figure 4.1b Particle size distributions for the 120 wheel grit number

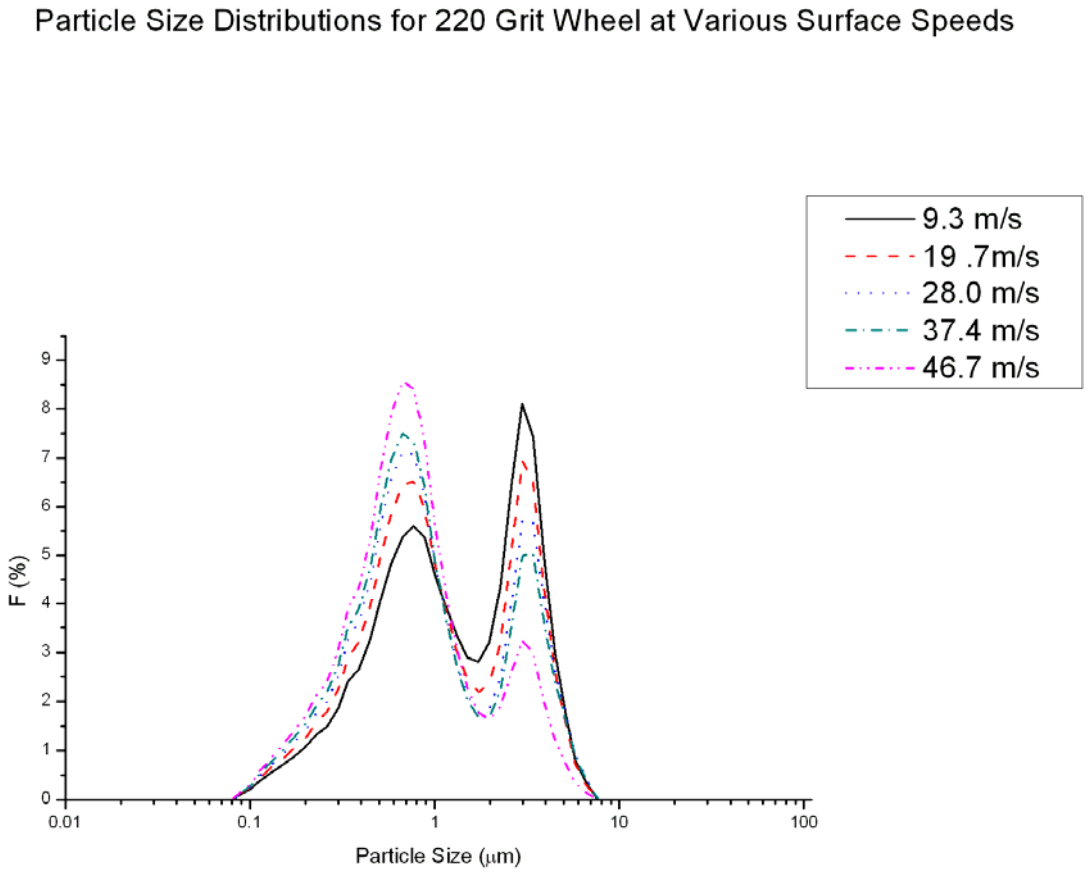

Figure 4.1c Particle size distributions for the 220 wheel grit number

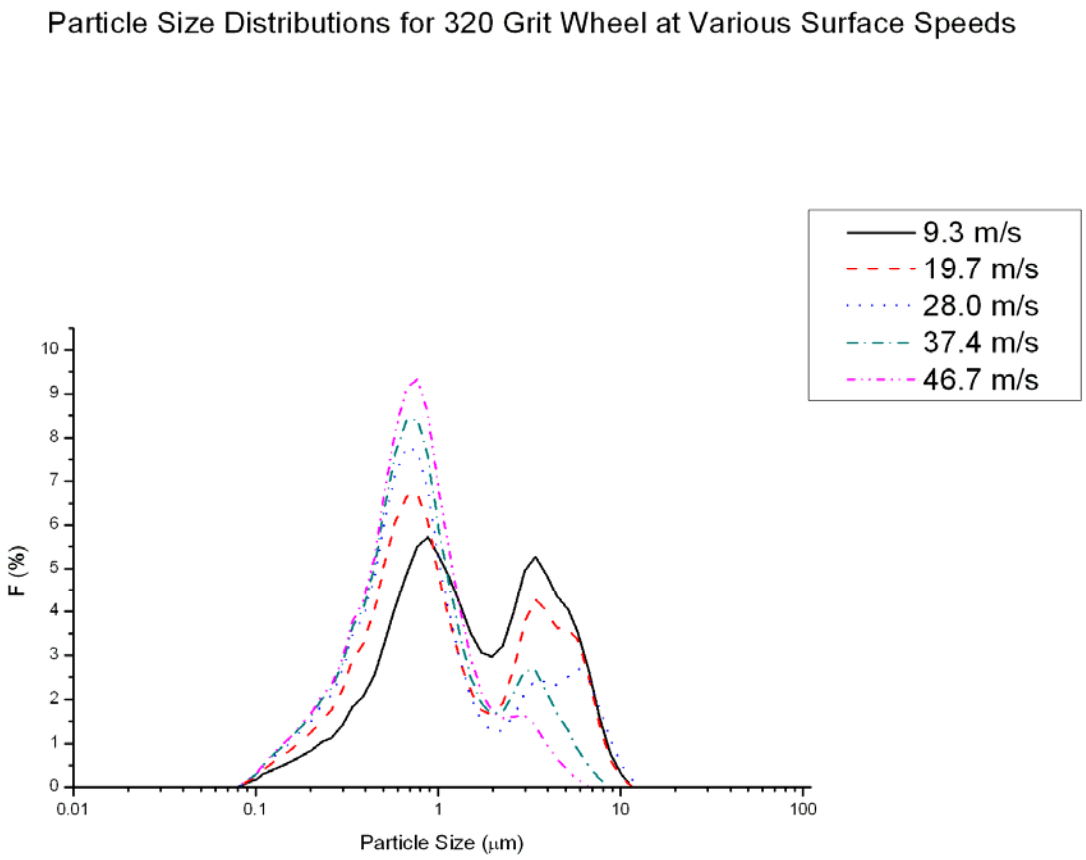

Figure 4.1d Particle size distributions for the 320 wheel grit number

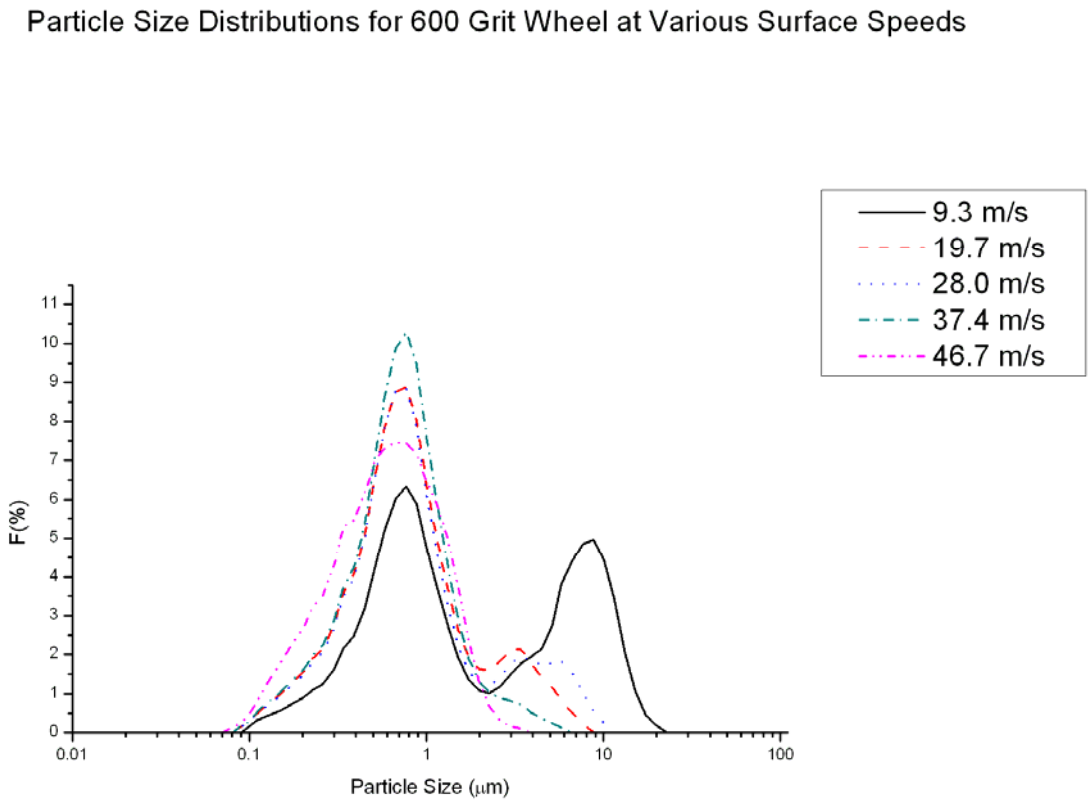

Figure 4.1e Particle size distributions for the 600 wheel grit number

The particle distribution plots for the various wheels and speeds show distinctly bimodal distributions for all but the highest surface speeds and finest grit wheels. In these distributions the coarse particle peak is centered in the 6 to 7 micron region and a finer peak is centered in the 0.3 to 0.6 micron region. The relative proportions of the coarse and fine peaks in the particle size distributions appear to be determined predominantly by wheel speed, with increasing surface speeds producing a greater number of finer particles and a reduction in the apparent number of coarse particles. Wheel grit also appears to play a role in determining the particle sizes, with the 600-grit number wheel ultimately resulting in the elimination of the peak denoting coarser particles at a surface speed of 37.4 m/s, while the other, coarser-grit grinding wheels utilized continued to generate bimodal distributions at even the highest m/s surface speed.

In order to further understand the shift of peaks in the particle size distribution as a function of surface speed, the plots were analyzed using log-normal curves fitted to the distributions obtained from the Horiba light scattering system. The nonlinear curve-fitting feature within OriginPro 7.5 was used to fit curves to the fractional particle size data points of each machining trial. The centers of these curves were obtained from the graphing program and integration of the curves as plotted on the frequency vs. log particle size using areas were carried out by graphical analysis in Adobe Photoshop.

The majority of distributions were best fit by three log-normal curves, one associated with the peak for coarser particles denoted as peak one and two for the finer peak denoted as peaks 2 & 3. Two peaks were utilized to fit the finer peak as the finest particles continually

fell outside of fits utilizing a single log-normal curve. The location of the peak centers and their relative percentage with respect to the total particle size distribution is shown in the Table 4.1.

Table 4.1 Fitted peak centers and their percentage of the total distributions

Wheel Grit Number	Wheel Speed (m/s)	Peak 1		Peak 2		Peak 3	
		Center (μm)	Percentage of total distribution	Center (μm)	Percentage of total distribution	Center (μm)	Percentage of total distribution
40/50	9.35	6.07	62	1.12	36	0.20	2
40/50	19.69	6.97	50	1.00	47	0.20	3
40/50	28.04	6.23	45	0.93	49	0.24	6
40/50	37.39	6.10	38	0.89	53	0.28	9
40/50	46.74	4.43	33	0.90	53	0.35	14
120	9.35	5.40	64	1.16	33	0.23	3
120	19.69	4.94	48	0.95	41	0.33	11
120	28.04	4.38	41	0.96	47	0.38	12
120	37.39	7.15	31	0.91	59	0.28	10
120	46.74	3.47	22	0.93	62	0.33	16
220	9.35	3.34	39	1.04	56	0.25	6
220	19.69	3.38	32	0.93	58	0.27	10
220	28.04	3.50	28	0.87	60	0.30	12
220	37.39	3.53	26	0.86	60	0.31	14
220	46.74	3.32	15	0.86	68	0.33	18
320	9.35	4.65	40	1.09	44	0.53	15
320	19.69	4.86	35	0.89	51	0.37	14
320	28.04	5.83	26	0.86	59	0.34	16
320	37.39	3.77	18	0.88	63	0.37	19
320	46.74	3.09	12	0.90	65	0.43	24
600	9.35	9.32	41	0.94	53	0.25	6
600	19.69	3.84	17	0.88	65	0.40	18
600	28.04	5.30	19	0.87	62	0.41	19
600	37.39	2.64	10	0.88	69	0.48	22
600	46.74	-	-	1.13	50	0.68	50

The general locations of these peaks are labeled for the case of the 40/50-grit number wheel in Figure 4.2. As is denoted in Table 4.1, the centers of these peaks shift somewhat over the range of wheel speeds examined in this research, but the region of the peak remains similar. For the case of the 600 grit number wheel at the 46.7 m/s surface speed, the particle distribution displayed in figure 4.1e shows the coarse particle peak has been completely eliminated. As the coarser particle peak is not present for this distribution it was found that the particle distribution of the 600 grit number wheel at 46.7 m/s was best fit by two peaks as opposed to the three used for the other particle distributions. Due to this

elimination of the coarser particle peak, the submicron region of the finer peaks of this distribution has in turn grown, resulting in the shift of the peak centers used to fit peaks 2 and 3 in table 4.1.

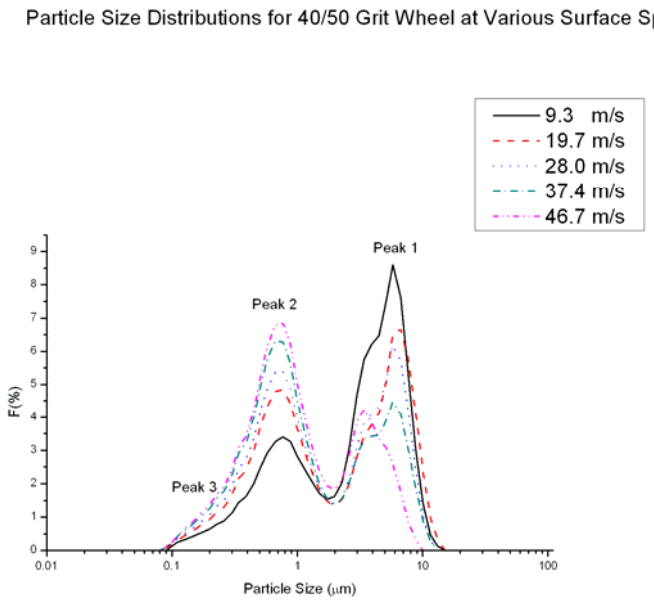

Figure 4.2 Locations of peaks for particle distributions generated by the 40/50 grit number wheel

The centers of the curves used to fit peak 1 are displayed below in Figure 4.4. For some wheels these peak centers appear to decrease in particle size with increasing surface speed. However, for most wheels the values for peak 1 vary wildly without any obvious correlation between particle size with grit size or surface speed. The exception seems to be the 220 grit number grinding wheel, where the coarser peak center remains almost constant; referring back to the waterfall plot show as figure 4.1c it is apparent that the 220 grit number wheel generates the only particle distributions that have a single distinct peak in the coarser

particle region. The remaining wheels display what appear to be multiple particle size populations in the coarse peak. This indicates that much of the variance in the peak 1 center for the other wheels results from the varying populations of particle sizes within the coarser region at a given surface speed.

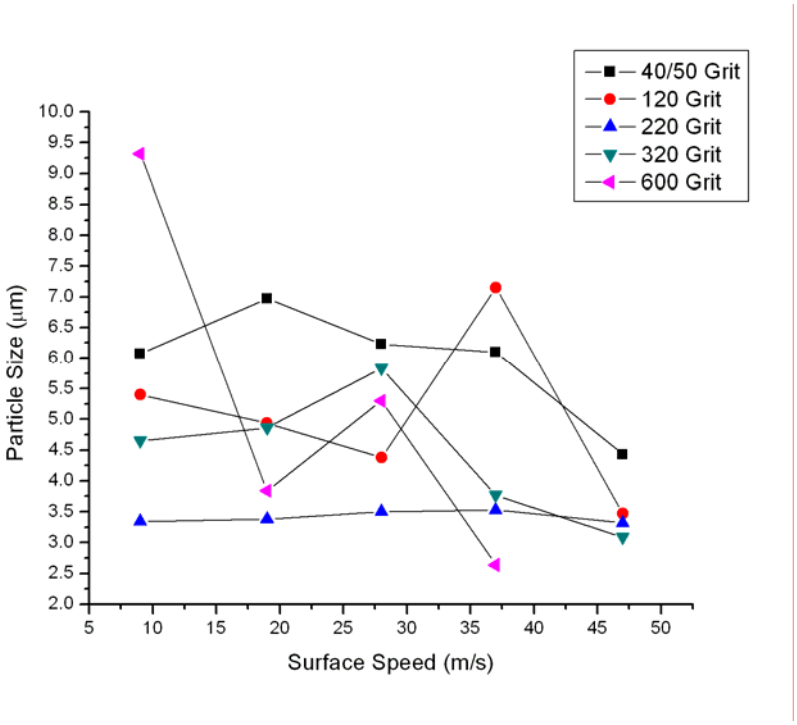

Figure 4.3 Plot of peak 1 fit centers vs. surface speed for various wheel grit numbers

The peak centers for peak 2 are plotted with respect to surface speed for the various grit number wheels used in this research in Figure 4.5. The typical trend for these values is a decrease with increasing wheel speed with three grit number wheels producing apparent increases in particle sizes at the highest wheel speeds. The degree of this shift is seen to vary with increasing wheel speed, where the shift in peak center between lower surface speeds is greater than that seen at higher ones. The highest surface speed peak center value for the 600 grit number wheel in this plot presents a significant break in this trend, this results

from the reduction of particle sizes into the peak 2 and peak 3 region. Increasing in peak centers for higher wheel grit centers could be due to greater compaction and agglomeration occurring at higher wheel grit or due to increased axial runout at higher wheel speeds.

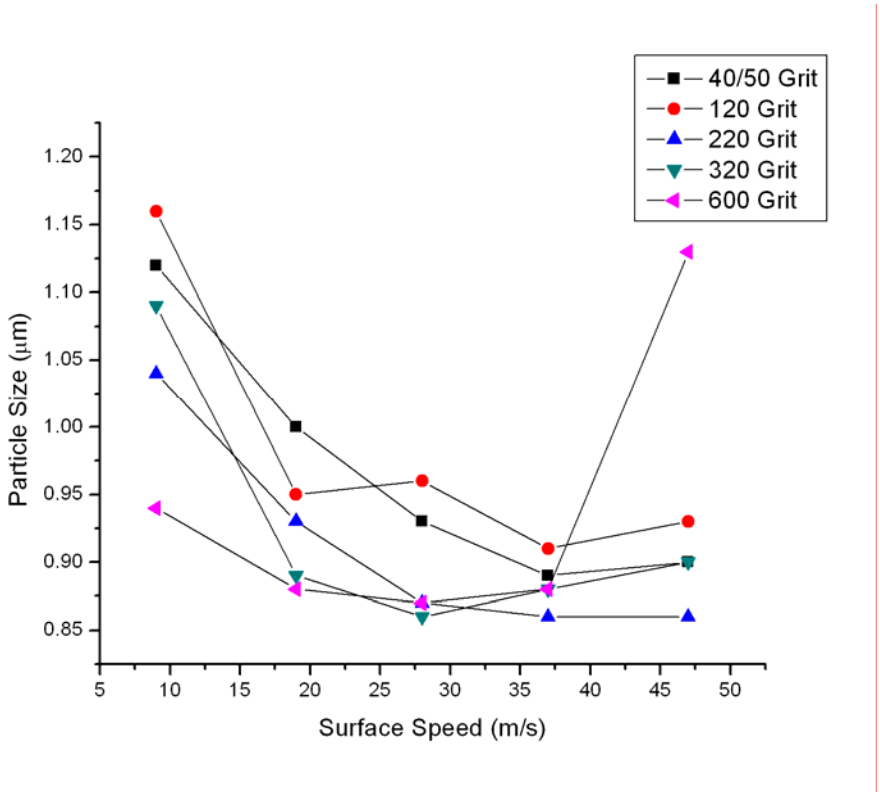

Figure 4.4 Plot of peak 2 fit centers vs. surface speed for various grit number wheels

The peak centers increase in size with increasing wheel speeds. The 320 grit number wheel displays an exception to this trend as in its case this peak center initially deceases in size and then begins to increase as surface speeds are increased above 27 m/s. These observed increases are due either to increased agglomeration of finer particles in this range of the particle distribution or to the variation in peak fitting as the finer particle sizes increased and do not indicate that higher wheel speeds generated fewer very fine particles.

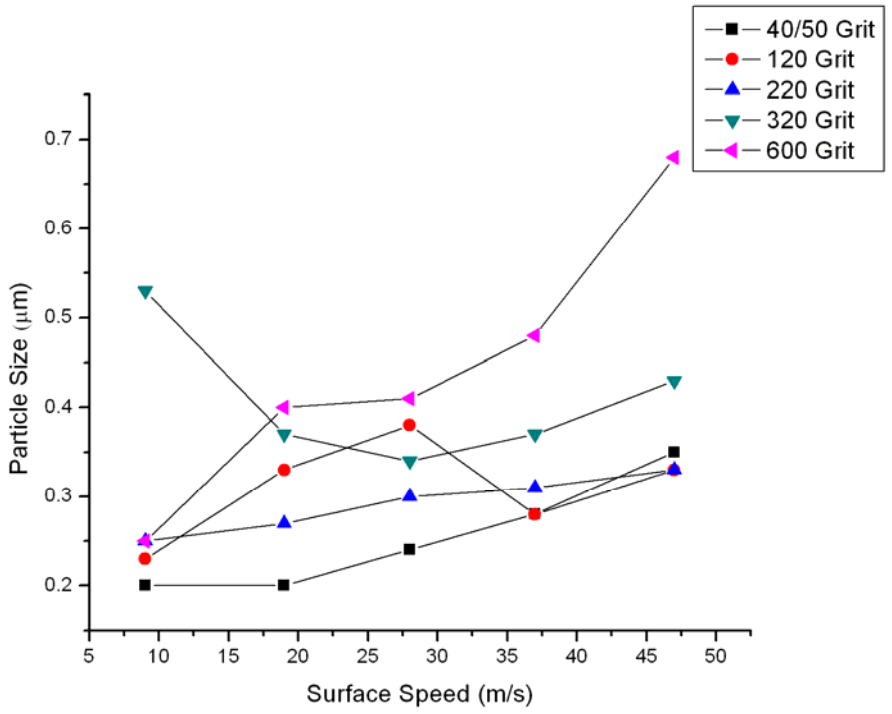

Figure 4.5 Plot of the peak 3 fit centers vs. surface speed for various wheel grits

As the distributions in Figures 4.1a-e and the analysis of the fitted peak centers in Figures 4.3-4.5 show, the decrease in mean particle size of the grinding swarf does not appear to be due to a shift of the peaks within the powder distributions. To investigate the shift of particles from one peak to another, the percentages of the particles in the peaks are plotted with respect to the size of abrasive particles in the grinding wheels for the examined surface speeds in Figures 4.6a-e.

These figures plot the shift from coarse to fine particle sizes observed in figures 4.1a-e, using the numerical values in Table 4.1. The plots show a growth in the size of peaks 2 and 3 and a decrease in the size of peak 1. In conjugation with the Figures 4.3-4.5 it is

observed that the majority of particle size reduction occurs as a transfer of particles from the coarser peak to the finer peaks as opposed to a shifting of the peaks with varying wheel speed and abrasive particle size. This shift is most prominent for the highest two surface speeds where the coarsest peak is either nearly eliminated or completely reduced to finer particle sizes. At these higher surface speeds sufficient energy and machining rates facilitate reduction in the scale of fracture in the workpiece to completely eliminate the coarser particles found in the particle distributions.

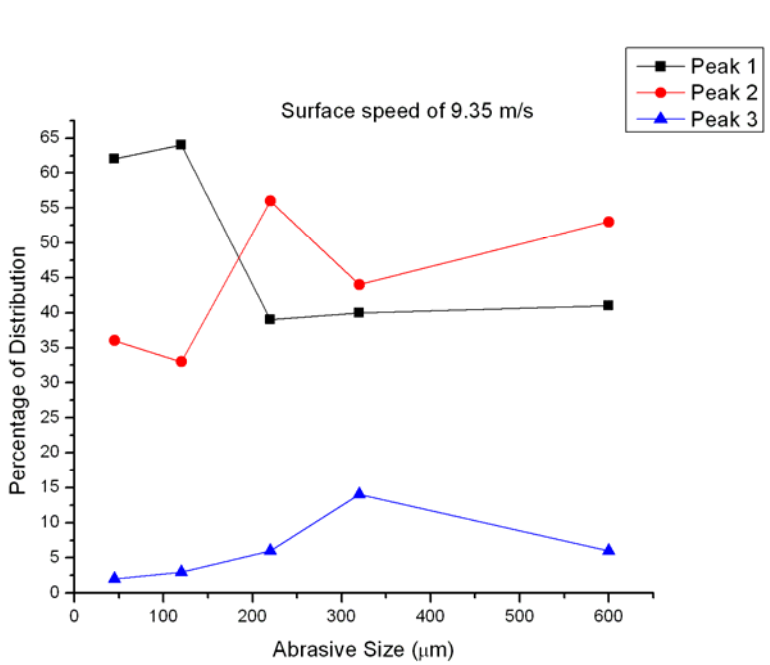

Figure 4.6a Relative size of peaks at .3m/s surface speed

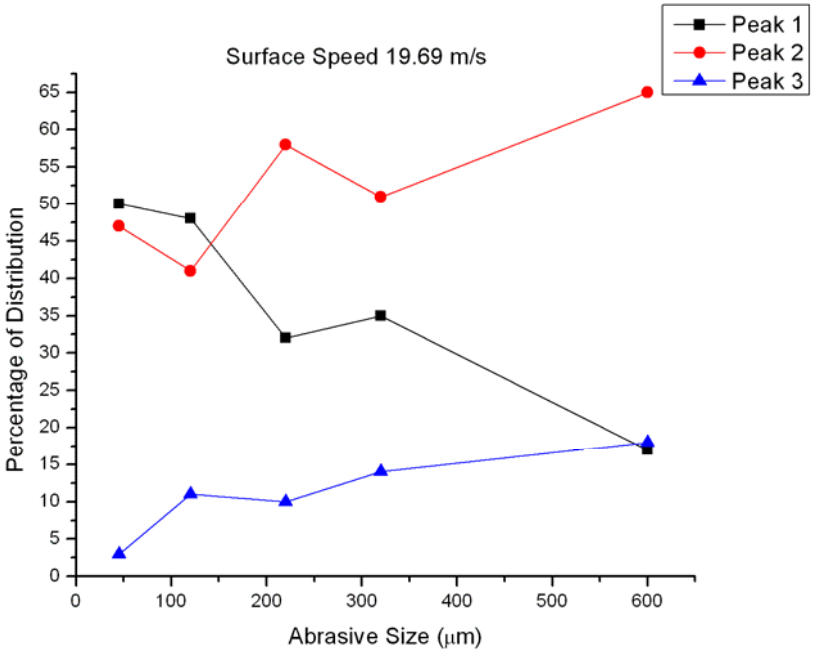

Figure 4.7b Relative size of peaks at the 19.7 m/s surface speed

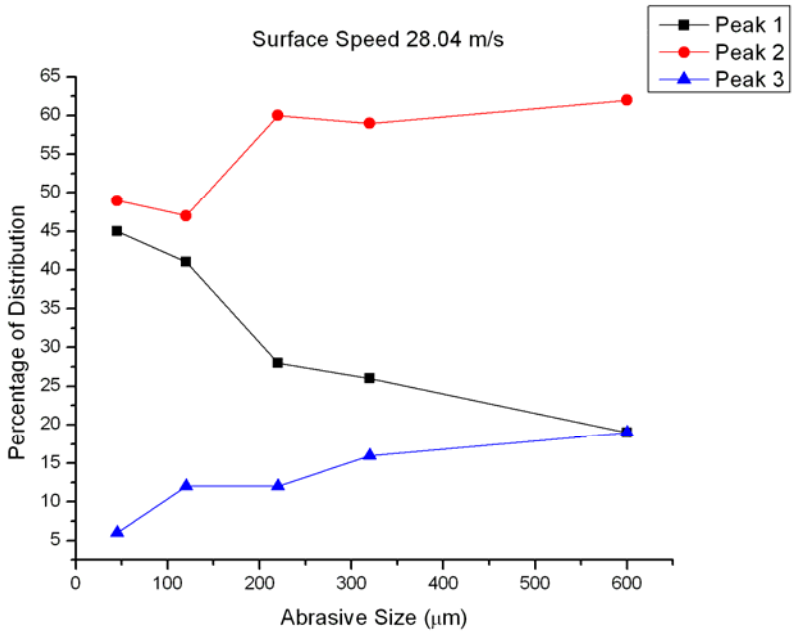

Figure 4.6c Relative size of peaks at the 28.0m/s surface speed

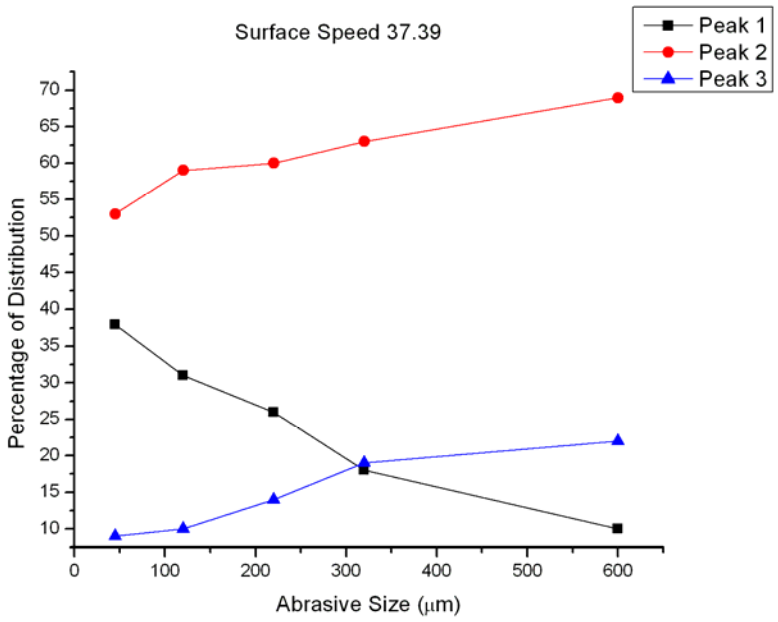

Figure 4.6d Relative size of peaks at the 37.4m/s surface speed

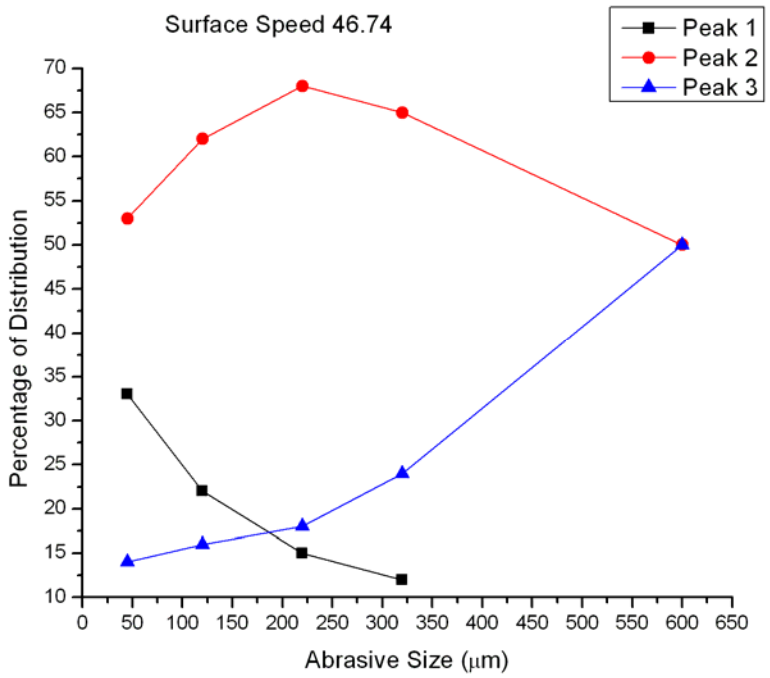

Figure 4.6e Relative size of peaks at the 46.7m/s surface speed

4.2 Mean Particle Size Data

In addition to the particle distribution data, the Horbia LA-700 particle size analyzer provided mean particle size data for each swarf sample. These values are based on particle count, like the fractional particle size plots shown earlier, and therefore are numerical not mass averages. The mean particle sizes for each grinding trial using the silicon carbide sample are displayed below in Figure 4.8.

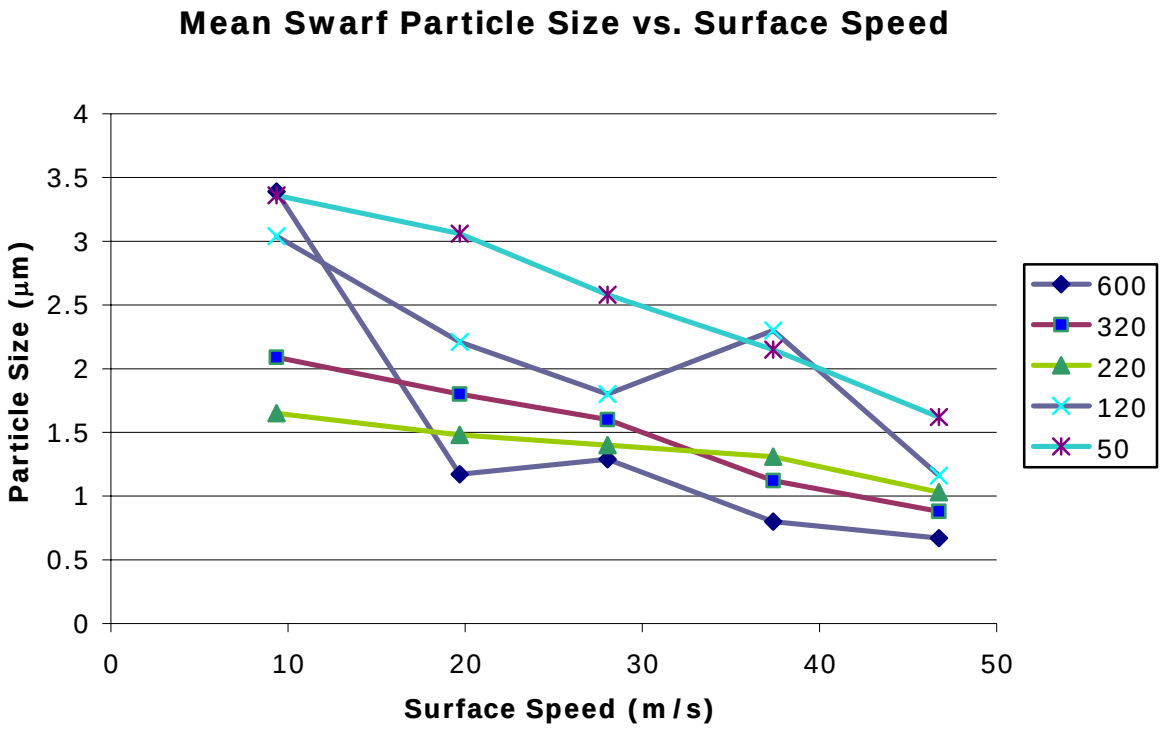

Figure 4.8 Plot of mean particle size data vs. surface speed for the silicon carbide sample

With the exception of a few data points, the data displays a linearly decreasing mean particle size with increasing grinding surface speed. The most notable exception is the distribution of the 600 grit number wheel at 9.3 m/s, which represented the largest mean particle size of all the grinding trials and as the previous peak fitting data displayed, the large mean particle size is due to a shift in the coarsest particles to larger sizes. This drastic deviation could have resulted from wheel degradation due to the high grinding forces experienced at low wheel speeds or from large scale chipping of the workpiece as a result of the diffuse force applied to its surface by the numerous cutting points and low wheel speed of this trial.

As indicated by Figure 4.8, wheel grit also appears to play an important role in determining the swarf particle size. Examining the mean particle data wheels having higher grit designations generate a finer series of mean particle sizes. The most significant deviations from the trend of decreasing mean particle size with increasing wheel grit designation are the 9.4 m/s 600 grit number wheel trial and the 28.0 m/s 120 grit number wheel trial. As stated previously the larger mean swarf particle size of 9.4 m/s 600 grit number wheel trial appears to be due to larger particle fracturing off the workpiece or grinding wheel due to non-optimum grinding conditions. The 28 m/s 120 grit trial appears to be an outlier in the experimental data and can not be readily explained.

The transition of the 320-grit wheel from initially generating coarser swarf particles than the 220-grit grit wheel and eventually finer particles at high surface speeds could be due to the change in wheel diameters moving from the 320 to 220 grit number wheels from 5 to 6 inches. As indicated by the grit depth of cut equation (2.1) a decrease in the wheel diameter also results in a decrease in the grit depth of cut. For different diameter wheels the applied force remains constant at a given surface speed and the interaction volume between abrasive grit and workpiece material is decreased as the wheel diameter is decreased.

Using the estimated grit density values of 4, 8, 16, 35, 120 cutting points per millimeter squared for the 40/50, 120, 220, 320, and 600 grit number wheels respectively the grit depth of cut equation (2.1) was plotted with respect to surface speed in Figure 4.6. The scale of these values and their trending reduction corresponds closely with the trends and values observed in the fitted peak centers of peak 2. With the exception of the two high surface speed values that shifted to coarser particle sizes, the fitted peak centers for peak 2

follow the same trend as the grit depth of cut. However, the peak center particle sizes are coarser than predicted by the grit depth of cut equation suggesting, as would be expected that fracture on a scale larger the physical depth of the abrasive particles in the workpiece.

In all cases but the 40/50 grit number wheel the particles formed are larger than predicted by the grit depth of cut equation. The ratio between the theoretical depth of cut and the observed particle size follows a linear relationship with increasing wheel speed and becomes larger with increasing wheel grit number. The scale of this fracture is most likely specific to wheel, workpiece, and machining parameters, but clearly indicates the particles generated are consistently larger than would be predicted by the grit depth of cut equation.

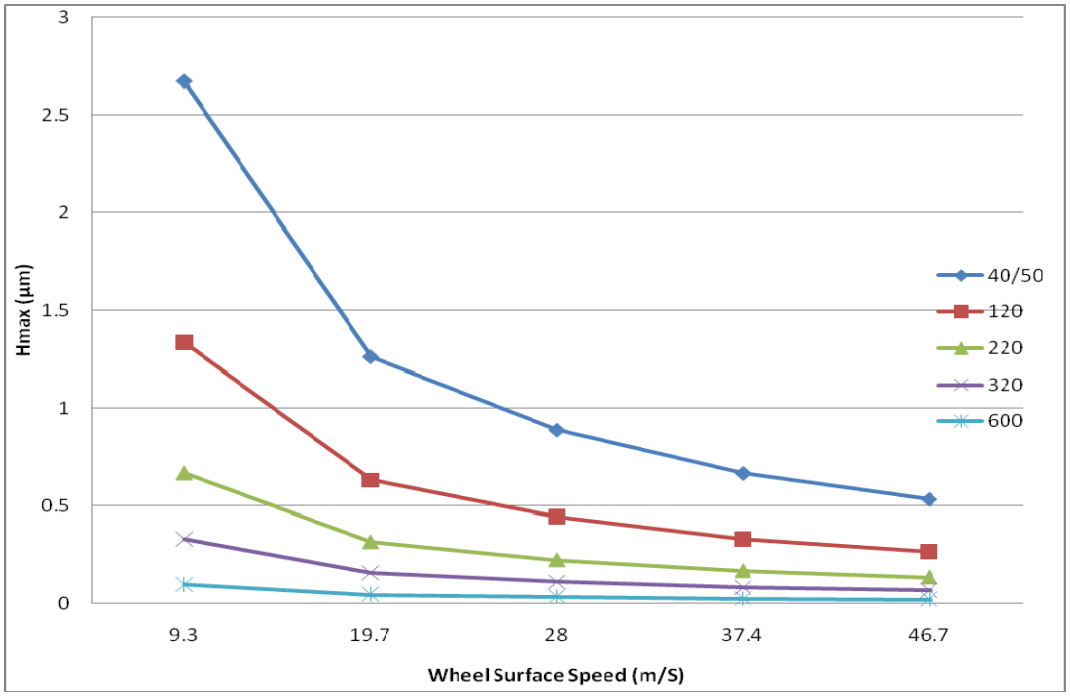

4.8 Plot of Grit Depth of Cut in Relation to Wheel Surface Speed

4.3 Single-Grit Pendulum Scratch Test

A single-grit pendulum scratch test conducted at Oak Ridge National Laboratory allowed for calculation of the specific energy of removal during a scratch generated with a diamond indentor. An optical micrograph of the resulting scratch is displayed in Figure 4.9. The scratch occurred from left to right and is approximately 1.22mm in length. The small extraneous scratch to the left of and slightly below the main scratch is believed to have occurred during the indentor alignment in the testing apparatus and was ignored for the purpose of this work. Regions of increased material removal resulting from lateral cracking induced by the force of the indentor are seen along the length of the scratch.

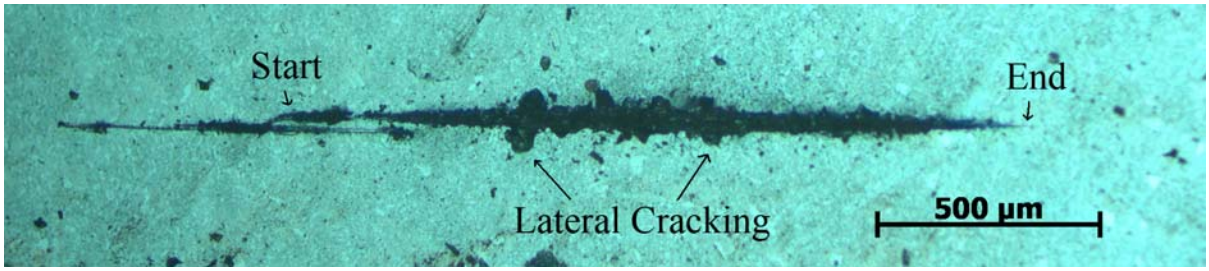

Figure 4.9 Optical micrograph of single-grit pendulum scratch on silicon carbide

The scratch was further analyzed with a Rodenstock RM-600 laser profilometer, which provided a 3-D scan of the scratched region shown in Figure 4.10. The scan found the deepest portion of the scratch to be a region extending roughly 20 micrometers below the surface with the majority of the scratch being approximately 10 micrometers in depth. The base of the scratch appears very irregular in the surface scan. This is attributed to the cracking and possibly difficulty in obtaining signals from areas with very steep sidewalls.

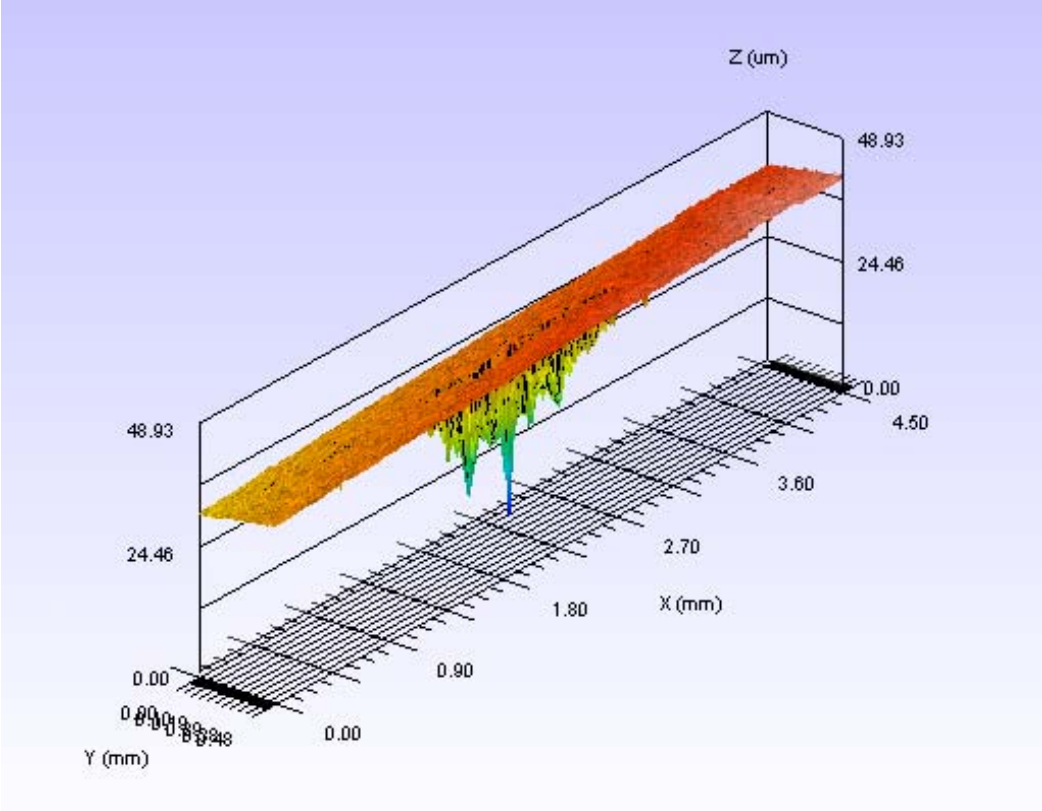

Figure 4.10 Laser profilometry surface scan of scratch

In order to determine the cross-sectional area removed along the length of the scratch the sample tilt in the scan data displayed in Figure 4.10 was removed from the coordinate data points and area data taken from each of the scans taken perpendicular to the scratch. The values obtained by these calculations are displayed in Figure 4.11. The effect of chipping during the scratching process is readily observed as peaks in the plot of area of material removed along the length of the scratch indicating, that chipping to the sides of the scratch increased the area removed by the passing indentor.

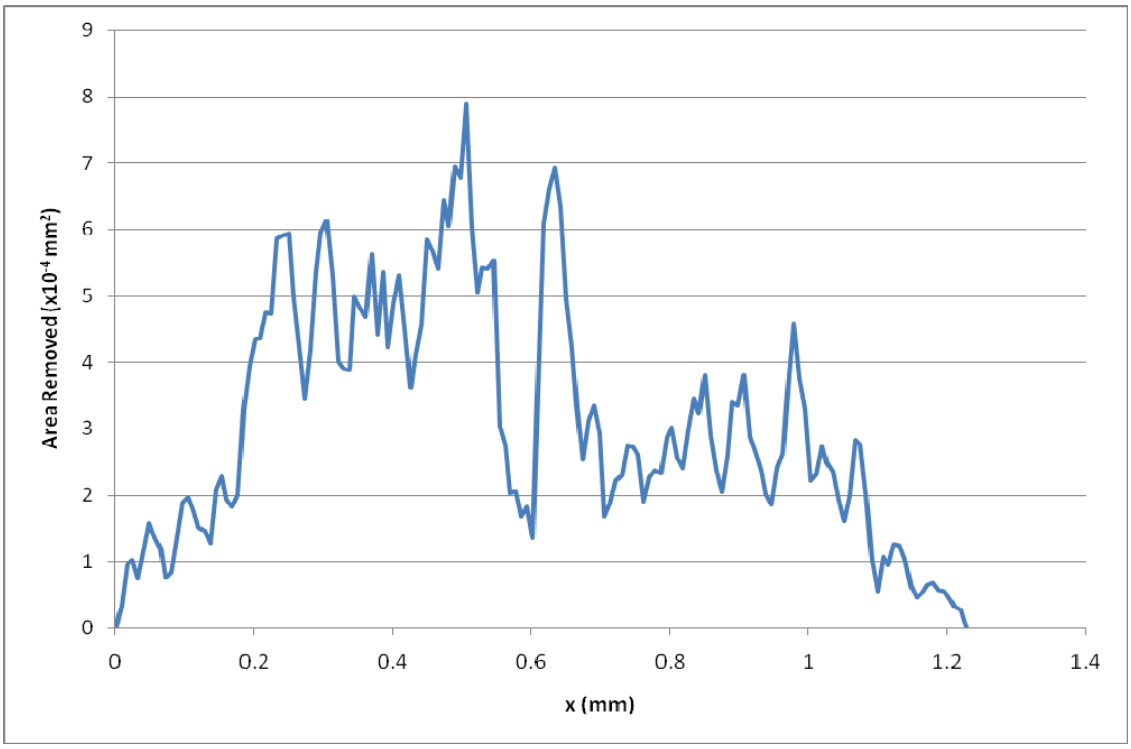

Figure 4.11 Cross-sectional area removed along the length of the scratch

Tangential and normal forces with respect to the moving indentor were recorded by load cells mounted on the specimen holder at a rate of 10^6 Hz and these forces were correlated to positions along the length of the scratch as displayed in Figure 4.12. Tangential forces remained below the normal forces for the duration of the scratch and significant drops in the two force curves coincided across the length of the scratch. This is in agreement with grinding experiments by Koepke and Stokes on MgO, where horizontal grinding forces remained constant over a variety of depths of cut while normal forces increased significantly with increasing depths of cut. [35]

Comparing the position of these decreases in the force curves to positions on the cross-sectional area of material removed curve showed that the minima occurred at about 0.5

mm and 0.7 mm from the beginning point of the scratch. These force decreases seem to coincide closely with drops in the cross-sectional area removed curve. This is attributed to spikes in force immediately before chipping events followed by a decrease in the force needed to travel through material that has been chipped away ahead of the passing indentor.

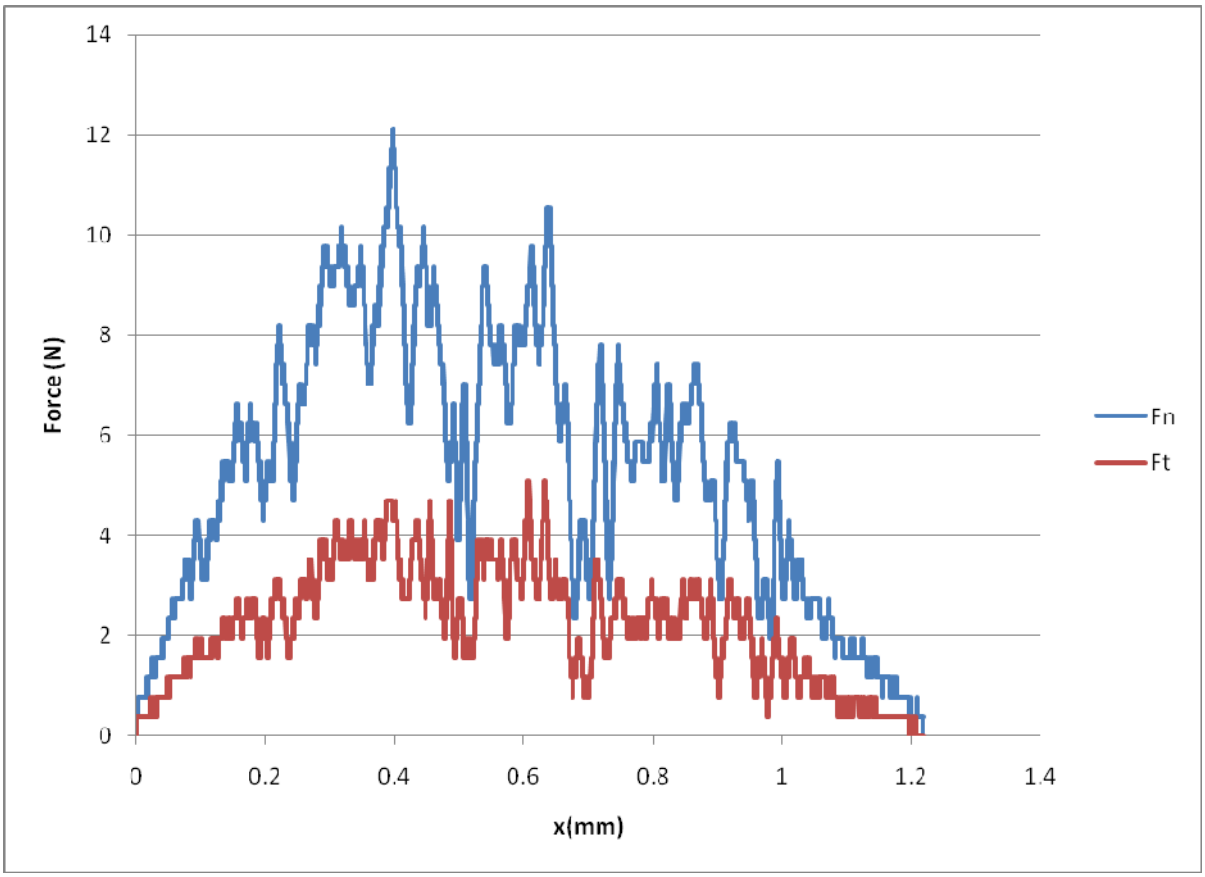

Figure 4.12 Normal and tangential force curves over the length of the scratch

The instanteous specific energy (S_e) for material removal is given by the following relation of tangential force (F_t) and cross-sectional area removed (a_r).[33]

$$S_e = \frac{F_t}{a_r} \qquad 4.2[33]$$

Using this relation, a plot of the specific energy over the the scratch length was formed and is shown in Figure 4.13. The intial peak in specific energy at the start of the scratch and the lesser peak at the end of the scratch result from the decreased depth of cut relative to the rest of the scratch. This decreased cut depth at the beginning and end of the scratch was due to the pendulum motion of the indentor. These peaks in specific energy is an example of the "size effect" is attributed to a shift from plastic deformation processes to brittle fracture as the depth of cut is increased by the arced path of the moving indentor.

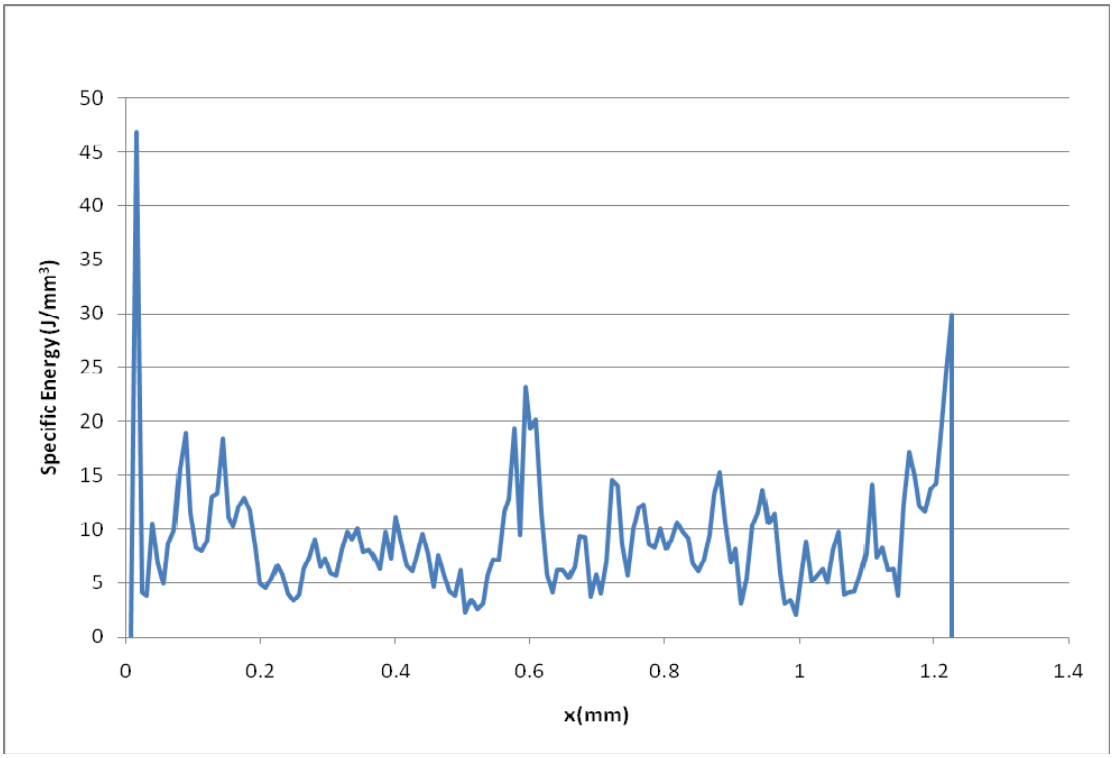

Figure 4.13 Variation in specific energy along the length of the scratch

4.4 Energy Dispersive Spectroscopy

Energy Dispersive Spectroscopy (EDS) was performed in a Hitachi S-3200N SEM on swarf particulate samples from both the metal and resin-bonded grinding wheels to look for differences in swarf composition. Figure 4.14 displays the EDS spectrum from particulate generated by grinding the silicon carbide sample at a surface speed of 19.7 m/s with the 40/50 metal bonded diamond grinding wheel. The spectrum is dominated by the silicon k peak. The presence of significant amounts of oxygen suggested some oxidation of the silicon carbide particles during their processing and storage. The large calcium peak is attributed to contamination in the grinder from conventional grinding wheels that use calcium as a binding material or from the water used as coolant during the grinding runs. The coolant water is also the likely source for the small chlorine and sodium peaks in the spectrum.

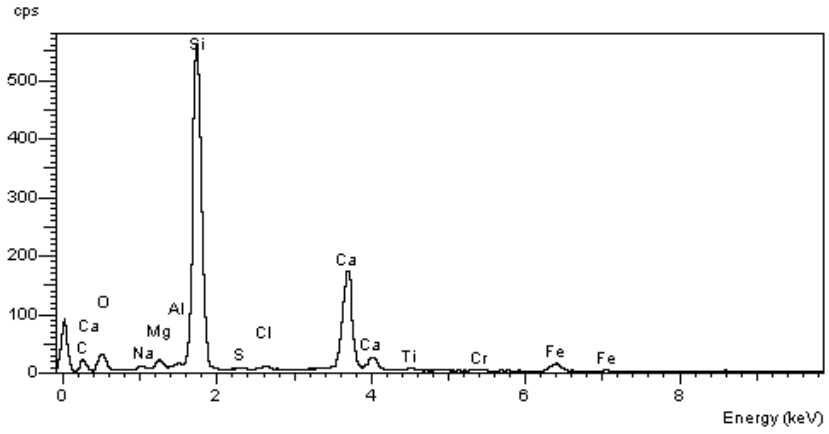

Figure 4.14 EDS spectrum taken from powder sample ground with the 40/50 grit wheel

For comparison, Figure 4.15 shows a similar EDS taken for silicon carbide generated by grinding with the 600-grit resin-bonded wheel at a surface speed of 37.4 m/s. The significant difference between the two spectra is the absence or reduction of some of the trace metals, such as titanium, chromium, and iron that is attributed to the lack of a metal binder in this grinding wheel. The calcium peak is also present in this grinding swarf sample and at a level equal to that found in the spectrum of the coarser wheel at a slower surface speed. The lack of variation in calcium content between wheel types and speeds supports the theory that the calcium comes from a contamination source and is not attributable to the workpiece or wear of the grinding wheels.

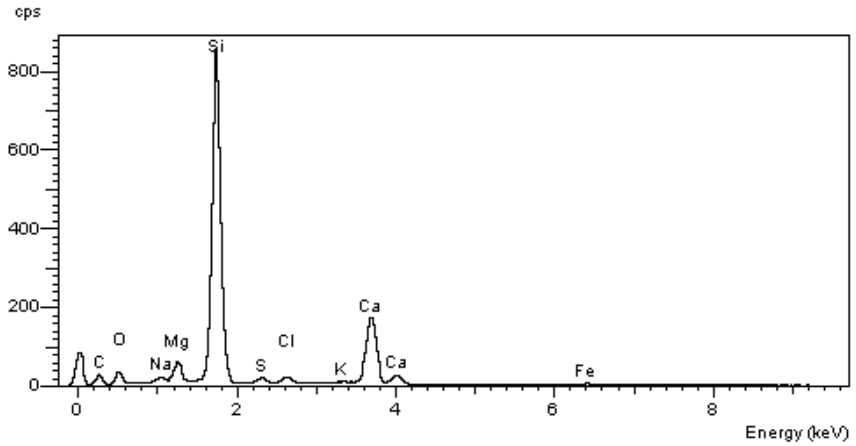

Figure 4.15 EDS spectrum taken from powder ground with the 600 grit wheel

4.5 TZP Grinding Trial

The TZP particle distribution for the tetragonal zirconia polycrystal material ground with a 600 grit number wheel at a surface speed of 46.7 m/s is displayed in Figure 4.16. Although this material had a uniform matrix grain size of roughly 200nm, its grinding resulted in a mean swarf particle size of 1.18 μm, which is larger than the mean swarf particle size for silicon carbide ground under the same conditions. The particle size distribution also appears to have a narrower distribution than the particles generated by the grinding of silicon carbide under the same conditions. A small proportion of particles appear to fall outside of a log-normal distribution on the in the 0.1 to 0.3 micrometer size range. This indicates a similar, albeit much less prominent bimodal nature to the particle distribution.

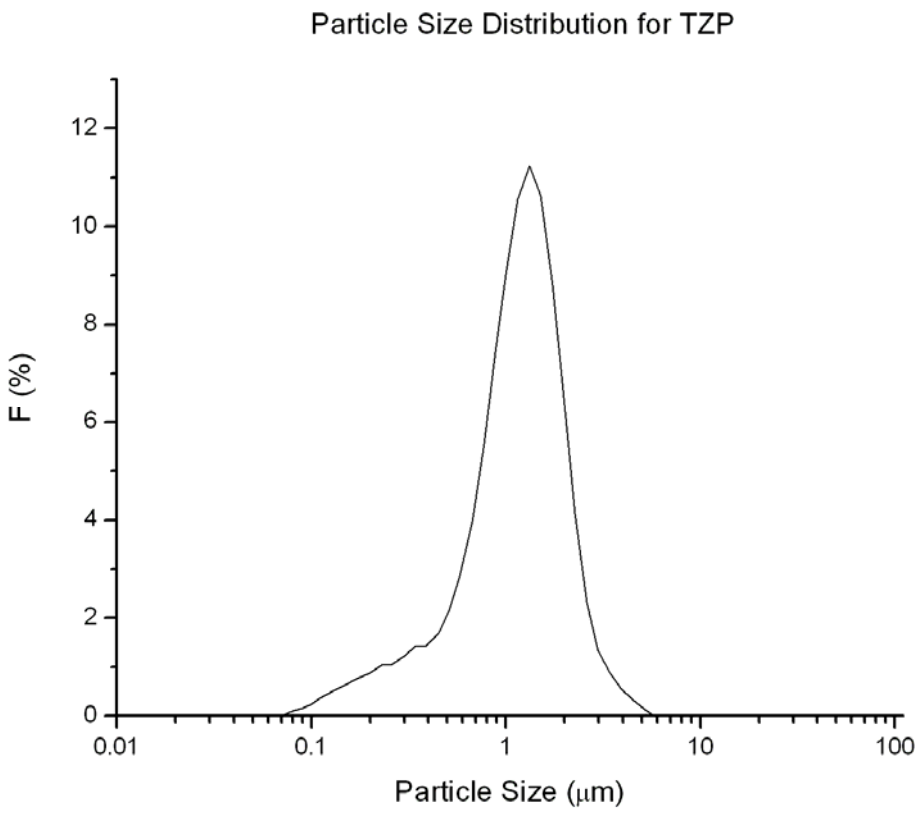

Figure 4.16 Particle size distribution for TZP grinding trial

The SEM micrograph of Figure 4.17 taken of the resulting tetragonal zirconia polycrystal particulate formed during grinding showed the material tended to generate chips reminiscent of those found in the machining of metals as is seen below in Figure 4.18. The particle in the center of the image appears, by its morphology, to be a continuous machining chip, similar to other chips observed throughout the powder sample. The edges and surfaces of a majority of the swarf material show fine features suggestive of a significantly finer grain structure with in the observed particles. The features appear to be on the scale of the 0.1 to 0.3 μm

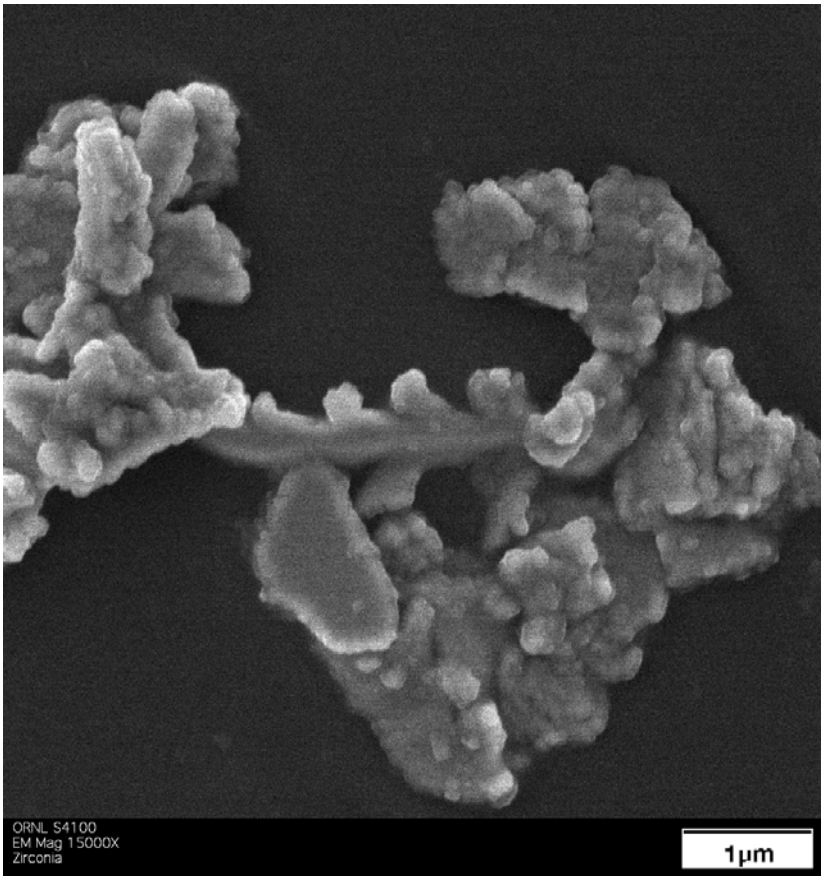

Figure 4.18 SEM micrograph of ductile behavior in TZP grinding chip

4.6 Analysis of Alumina Grinding Swarf from an Industrial Waste Stream

Samples of alumina grinding swarf taken from Blanchard grinding processes were similarly analyzed by light scattering analysis. The particle size distribution is displayed below in Figure 4.18. The resulting distribution was similar to other high speed grinding trials carried out in this study, yielding a mean particle size of 1.15 micrometers with no

particles larger than 5 micrometers. The 0.2 micrometer region of the distribution again deviates from a standard log-normal distribution suggesting a small peak in the finer region of the distribution.

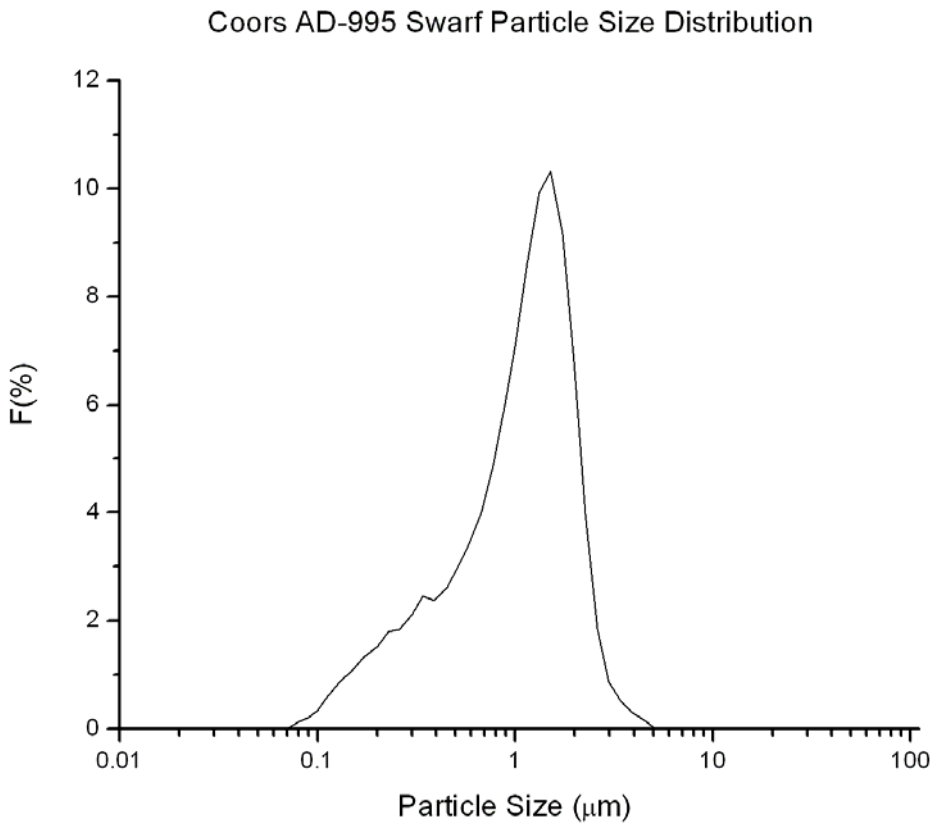

Figure 4.18 Particle size distribution for Coors alumina swarf

SEM analysis of particles generated during Blanchard grinding process showed what appear to be numerous fine particles agglomerating to with each other or to larger particles. The SEM micrograph shown as Figure 4.19 is representative of the swarf particles observed.

These particles appear to be small enough to suggest that the particle distributions observed via light scattering are not representative of a fully deagglomerated powder state.

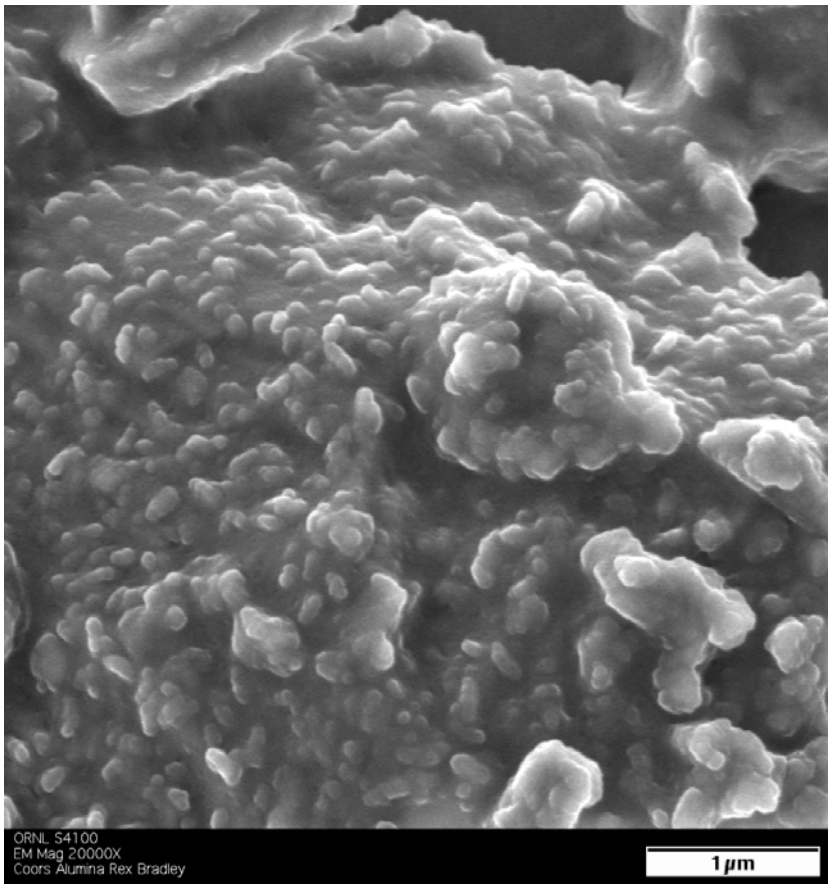

Figure 4.19 SEM micrograph of Coors alumina swarf

4.7 Efforts to Sinter Powder Reclaimed from the Grinding Swarf

The swarf generated from industrial grinding of alumina material was first baked as described in the experimental procedure section in order to evaporate hydrocarbons stemming from corrosion inhibitors in the cutting fluid. To this powder 1.5 wt% MgO was added in order to serve as a sintering aid. This mixture was placed in a plastic container with alumina balls and milled on rollers for a period of one hour.

The powder was pressed and sintered at Oak Ridge National Labs by Shirley Waters. This alumina material was first cold pressed into green pellets and then the green pellets were sintered at 1500$^{\circ}C$ and 1600ºC in air for an hour. Two additional pellets were hot pressed at 1500$^{\circ}C$ and1600$^{\circ}C$ respectively for two hours at a pressure of 40ksi.

Archimedes density measurements where performed to determine the effectiveness of these sintering methods on the swarf powder. Sintering of the cold pressed pellets yielded densities of 3.02 g/cc and 3.23 g/cc. Measurements taken on the hot pressed pellets found densities of 3.32 g/cc and 3.73 g/cc, the best of which being 93.7% of the theoretical density of alumina.

5.0 DISCUSSION OF RESULTS

The following evaluation of the results of the work will include a discussion of the bimodal nature of particle size distributions generated by surface grinding. The fitted mean particle data will be examined as a possible means of extrapolating to higher surface speeds and wheel grits. Lastly, the grinding data from other materials and potential for reuse of particulate material in the grinding swarf will be discussed.

5.1 The Nature of Bimodal Distributions Generated by Surface Grinding

All grinding trials on silicon carbide material carried out in this work showed a tendency toward bimodal particle size distributions, with a shift toward finer particle sizes as wheel speed increased and abrasive particle size decreased. A similar effect is seen in comminution processes, where crushing or grinding generate a polymodal distribution shifting towards a finer monomodal distribution as the feed material becomes increasingly fractured. [36] In the case of grinding, faster wheel speeds and finer abrasive particles impart energy into a localized area furthering the comminution process.

While the silicon carbide workpiece material displays a bimodal grain size distribution due to its production by a seeded growth process, the volume fraction of the seeding particles in the silicon carbide appears insufficient to produce the number of coarse particles seen in the particle distribution curves. Wear of the grinding wheels is also an unlikely source for either of the peaks in the particle distribution as it is assumed not to occur on the a scale needed to generate a significant fraction of the number of particles than were removed from the surface of the workpiece, as would be necessary for some of the size distributions particles where coarse particles dominate.

Presumably, the bimodal particle nature of the particle distribution is primarily due to a difference in the scale of fracture processes between coalescence of larger scale cracking resulting in chipping and finer scale fracture, popularly termed as crushing. The crushing and coalescence of lateral and median cracking damage mechanisms are influenced by both the grit depth of cut and the grinding forces exerted on the workpiece during the grinding process. The relative extent by which material is removed by either crushing or larger scale

median and lateral crack coalescence is believed to be responsible for the shift from the coarser peak to the finer peak of the particle distribution.

5.2 Effect of Surface Speed on Particle Size Distributions

Examination of the maximum undeformed chip thickness (h_{max}) equation discussed in the background section of this work, shows that the undeformed chip thickness is linearly related to wheel speed. As this equation dictates, the thickness of chips removed strictly by examining the thickness of material presented to the passing abrasive grit on a circular grinding wheel decreases with increasing wheel speed. During the majority of grinding taking place on brittle materials removal of material is likely to be dominated by brittle fracture as opposed to cutting mechanisms needed to remove material according to the maximum undeformed chip thickness geometry. However, the thickness defined by this equation does set the interaction volume between abrasive particles in the grinding wheel and the workpiece material.

Grinding trials carried out in this research allowed for development of a relationship between the calculated undeformed chip thickness and experimentally measured swarf particle size. These results support the conclusion that decreased penetration by grinding abrasives with higher surface speeds reduced the large scale fracture events which would generate coarser particles. The decreased grit depth of cut also means that grinding energy is dissipated within a smaller volume of chip material and more energy is available to propagate the small scale fracture events necessary to generate finer particles in the machining swarf.

Higher grinding wheel surface speeds also result in an increase in the number and velocity of abrasive particles making contact with the workpiece surface for a given time period. Increased wheel surface speeds correspond to increased loading rates, which in fragmentation studies of silicon carbide by Lankford and Blanchard have been shown to generate finer particles. [37] In addition, given an increased density of encounters between wheel abrasives and the workpiece at higher surface speeds, a larger portion of the workpiece material is subjected to the region directly under the moving diamond abrasive grit where stresses are largest and the greatest damage occurs.

5.3 Effect of Wheel Grit on Particle Size Distributions

Increasing grit number of the grinding wheel also affects final powder size distributions; with higher grit number wheels containing finer abrasive particles resulting in fewer coarse particles than those generated by lower grit number wheels with correspondingly coarser abrasives. The wheel grit number plays a role the undeformed chip thickness equation (h_{max}) through the active cutting point density term. Higher wheel grit numbers having finer abrasive particles have more cutting points for a given volume and therefore result in smaller values for the undeformed chip thickness when the abrasive concentration is held constant.

As with the decrease in undeformed chip thickness (h_{max}) caused by increasing wheel speed, increasing wheel grit designations result in a reduction in interaction volume between the grinding abrasives and the workpiece as well as a reduction in normal grinding force on the workpiece. Given higher abrasive grit concentrations a larger percentage of the

workpiece material will be exposed to the high stress directly under one of the abrasive cutting points on the grinding wheel. Both of these factors favor generation of finer swarf particles, which require finer scale fracture events.

5.4 Material Removal Mechanism during Scratching of Silicon Carbide

The single-grit scratch test on the silicon carbide material showed that during impact and scratching, similar to that occurring during surface grinding, material removal occurs due to brittle fracture resulting from the forces applied by the diamond indentor. Extensive lateral chipping during the scratch test corresponds to somewhat erratic behavior on the area removed and force curves as material is removed by brittle fracture ahead of the moving indentor. In addition the specific energy spikes at the beginning and end of the scratch correspond to the energy spike attributed to the "size effect" where shallow depths of cut induce more plowing and less material removal by fracture.

The spike seen in specific energy at very shallow depths of cut during the scratch test show that plasticity is increased at shallow depths of cut where plowing begins to add to the specific energy of grinding. This effectively limits the degree to which increasing wheel speed and decreasing abrasive particle size can reduce the size of swarf particles. Once the grit depth of cut is reduced to the point where plasticity takes a more dominate role in the deformation and fracture mechanisms occurring in the grinding process the effect of abrasive size and surface speed at reducing swarf particle through fracture will be reduced as a transition to ductile mode machining is made.

5.5 Generation of Fine Particles by Surface Grinding

Under the processing parameters examined this research effort was not able to generate a significant fraction of nanoscale particles using the available resin-bonded diamond grinding wheels and practical wheel speeds. The potential of using metal-bonded grinding wheels at higher surface speeds would allow for exploration of the relationship between surface speed and mean particle size. Following the trends observed in this research increased surface speeds should reduce the swarf particle size further.

5.6 Zirconia Particle Distribution Data

The grinding of tetragonal zirconia polycrystal (TZP) material resulted in a mean particle size of 1.18 μm. Grinding of silicon carbide produced under the same conditions resulted in a mean particle size of 0.67μm. Presumably, the lower hardness and higher toughness of the TZP material contributed to the increased swarf particle size.

The ductile chip formation, observed via SEM, is attributed to transformation-induced plasticity resulting from the tetragonal to the monoclinic phase transformation possible under the highly localized stresses generated by contact between abrasive particles in the grinding wheel and the material's surface. The phase transformation of TZP materials during surface grinding has been observed by Swain and Hannick for ceria-doped TZP.[38]

Relative to the silicon carbide material, the TZP material has a lower hardness indicating dislocation motion is easier and fracture processes less dominant in the material removal process. This would limit the scale of any particles generated by chipping from the

workpiece surface. The increased capability for deformation would also limit the degree to which particles in the coolant stream could be further crushed between the grinding wheel and workpiece surface.

5.7 Alumina Particle Distribution Data

As grinding of the alumina was carried out using a Blanchard grinding process, only qualitative comparisons can be made with the particle distributions of the silicon carbide. The particle distribution obtained for alumina grinding swarf is similar in nature to the distributions for the highest wheel speeds and highest grit value grinding trials carried out on silicon carbide. The finer particles that fall outside the log-normal curve fit of the largest peak indicate a multimodal particle distribution, as was found in the silicon carbide grinding trials.

All particles generated by grinding of alumina are below the six-micron average grain size for the material, indicating the occurrence of fracture on a scale below the grain size of the material occurring at some point during the grinding process. The scale of the particles generated by this grinding process can be attributed to crushing events causing intragranular fracture events which effectively crush workpiece grains into fine particles. While this industrial grinding process does significantly reduce the starting grain size of the workpiece only a very small faction of particles approached the realm of being nanoscale in size.

5.8 Reclamation of Industrial Grinding Waste

In the particular case of reclaiming Coors AD-995 alumina swarf from a Blanchard grinding process, the material was easily cleaned and cutting fluid contaminants were reduced. Efforts to sinter the reclaimed material resulted in densities ranging from 3.02 g/cc to 3.73 g/cc. This reclamation could be scaled to match the output from grinding processes and this material reused effectively mitigating a large portion of these processes waste streams.

6.0 CONCLUSIONS

Examination of particles collected from waste streams of ceramic grinding processes has shown their sizes to be on the micron to submicron scale depending on machining conditions and properties of the ceramic workpiece. Comparisons of particle distributions taken from various machining trials showed that increasing grinding speeds resulted in a shift of the resulting particle distribution from a distinctly bimodal distribution to a monomodal distribution with a mean particle size of 0.67μm. This shift in particle distributions is also observed to be influenced by wheel grit number, with increasing wheel grit numbers tending toward finer particle sizes. Should these trends continue to higher surface speeds it is expected that the particle sizes below 100 nanometers would be generated. These observations are based on surface grinding of silicon carbide using superabrasive grinding wheels. Other grinding methods and workpiece configurations may result in different relations.

This reduction in swarf particle size is attributed to the influence of wheel speed and wheel grit number on the depth of material presented to the grinding abrasives as dictated by the undeformed chip thickness equation (h_{max}). Increasing wheel speed and decreasing abrasive particle size both serve to decrease the thickness of material presented to abrasive particles on the grinding wheel. This in turn reduces normal grinding forces and decreases the likelihood of large-scale fracture events necessary for the formation of coarse particles. Results from this work confirm a relationship between the undeformed chip thickness equation with mean particle sizes being larger than the predicted value but following the same the same predicted trend

Wheel speed and abrasive size also have the effect increasing the density and rate of impacts between abrasive particles and the workpiece surface. This increases the probability that swarf particles originate from regions directly under a moving abrasive particle that are subjected to dense microcracking. It also increases the chance that larger particles formed from chipping of the workpiece may fracture further secondary impacts between the workpiece and wheel abrasive before being cleared of the machining region.

Comparisons of particle size distributions from swarf generated by the grinding of silicon carbide and tetragonal zirconia polycrystal showed that materials with higher toughness values and lower hardness values generat larger particle sizes. This is attributed to transformation induced plasticity and easier dislocation motion in lower hardness materials resulting in larger deformed chips as opposed to fine fractured particles. The increased

ductility of the TZP material was observed to result in the formation of more traditionally shaped grinding chips in comparison to the particles formed from by the grinding of silicon carbide.

Attempts at reclamation of ceramic chip material from cutting fluids used in industrial grinding processes show the potential exists for recycling of ceramic material from the waste streams of grinding processes. Pellets were obtained with densities ranging from 3.02 g/cc to 3.72 g/cc after limited attempts at sintering. This result presents a promising outlet for material that is currently being disposed of at the expense of the waste generator. While nanoscale particles were not readily generated it has been shown that this "waste" material can be utilized as starting powder to be sintered into ceramic parts.

7 FUTURE WORK

In the area of future work, utilizing workpiece material of a uniform grain size would be of interest to rule out differing fracture behaviors between the larger seeding alpha grains and finer grains in the silicon carbide material as a possible cause for the bimodal particle size distributions. Similar grinding studies conducted on a range of materials with different grain sizes would be useful in examining the effect of grain size on the scale of particle generation during surface grinding. The trials conducted with metal bonded wheels would safely permit the use of substantially higher wheel speeds, allowing for further study into the effect of surface speeds on swarf particle size. Higher abrasive content in the grinding

wheels and higher wheel grit designations would likewise present further data as to the effect of abrasive concentration on swarf particles. In addition, investigating the relative effect of depth of cut and feed rate on particle size distributions present in the grinding swarf would be of interest.

8 REFERENCES

1] Salmon, S. C. (1992). *Modern Grinding Process Technology.* McGraw-Hill Inc.

2] Malkin, S. (1989) *Grinding Technology Theory and Applications of Machining with Abrasives. P. 9* John Wiley & Sons.

3] Marinescu, I., Tonshoff, H., & Inasaki, I. (2000). *Handbook of Ceramic Grinding and Polishing.* Norwich: Will Andrew Publishing, LLC.

4] Marinescu, I., (1993). Tribological Aspects of Brittle Material Grinding. *Proc. Of Diamond 7 CBN Ultrahard Materials Symposium '93* Windsor, Canada

5] J.L., M. (1986). *Superabrasive Grinding.* Cambridge: Butterworth & Co (Publishers).

6] Kovach, J. A. (1993). A Feasibility Investigation fo High Speed Low Damage Grinding Process for Advanced Ceramics. In *5th International Grinding Conf., Vol 1, SME.*

7] Malkin, S., & Ritter, J. (1989) Grinding Mechanisms and Strength Degradation for Ceramics. *Journal of Engineering for Industry* , Vol.111. 167-174.

8] Jahanmir, S., (1995). Machining of Advanced Ceramics. *Tribology International* , Vol. 28, No. 6 pp. 415-420.

9] Strakna, T., Jahanmir, S., Allor, R., & Kumar, K. (1996). Influence of Grinding Direction on Fracture Strength of Silicon Nitride. *J. Eng. Mat. and Technol. 118:* , 335-342.

10] Jahanmir, S., Ramulu, M., & Koshy, P. eds. (1999). *Machining of Ceramics and Composites.* New York: Marcel Dekker, Inc.

11] Barsoum, M. (1997). *Fundmentals of Ceramics.* New York: McGraw-Hill Companies.

12] www.matweb.com

13] Bi, Z., Tokura, H., & Yoshikawa, M. (1988). Study on Surface Cracking of Alumina Scratched by Single-Point Diamonds. *Jounal of Materials Science* , 23 3214-3224.

14] Evans, A. G., & Marshall, D. B. (1981). Wear Mechanisms in Ceramics. In D. Rigney, *Fundamentals of Friction and Wear* (p. 439). ASME.

.

15] Xu, H. H., Jahanmir, S., & Wang, Y. (1995). Effect of Grain Size on Scratch Interactions and Material Removal in Alumina. *J. Am. Ceram. Soc* , 78[4]4 881-891.

16] Imanaka, O., Fujino, S., & Mineta, S. (1972). Driect Observation of Material Removal Process During Grinding of Ceramics by Micro-Flash Technique. In S. Schneider Jr., & R. Rice, *The Science of Ceramic Machining and Surface Finishing I NBS Special Publication No. 348* (p. 37). Washington: National Bureau of Standards

17] Zu, H., Padture, N. P., & Jahanmir, S. (1995). Effect of Microstructure on Material-Removal Mechanisms and Damage Tolerance in Abrasive Machining of Silicon Carbide. *Journal of the American Ceramic Society 78 (9)* , 2443-2448.

18] Zhang, B., & Howes, D. (1994). Material-Removal Mechanisms in Grinding of Ceramics. *Annals of the CIRP Vol. 43/1* , 305-308.

19] Hockey, B. J. (1972). Observations on Mechanically Abraded Aluminum Oxide Crystals by Transmission Electron Microscopy. *The Science of Ceramic Machining and Surface Finishing* (pp. 333-339). Gaithersburg, Md: National Bureau of Standards Special Pub. 348

20] Cutter, I., & McPherson, R. (1972 Vol.2 56 No.5). Plastic Deformation of Al_2O_3 During Abrasion. *Journal of The American Ceramic Society* , 266-269.

21] Bifano, T. (1988). *Ductile Regime Grinding of Brittle Materials.* PhD thesis North Carolina State University

22] Reichenbach, G., Mayer, J., Kalpakcioglu, S., & Shaw, M. (1956). The Role of Chip Thickness in Grinding. *Trans. ASME 18* , 847-850.

23] Koepke, B., & Stokes, R. (1972). Grinding Forces and the Machining of Magnesium Oxide Crystals. *Journal of Materials Science* , 485-493.

24] Inasaki, I. (1987). Grinding of Hard Brittle Materials. *Annals of the CIRP 36(2)* , 463-471.

25] Koepke, B. a. (1974). Grinding Damage in Ceramics. *Naval Research Reviews, 27, 1* .

26] Salmon, S. C. (1992). *Modern Grinding Process Technology.* McGraw-Hill Inc.

27] Hwang, T., & Malkin, S. (1999). Grinding Mechanisms and Energy Balance for Ceramics. *Trans. ASME, Journal of Manufacturing Science and Engineering Vol. 121* , 623-631

28] Hwang, T., Evans, C., & Malkin, S. (1999). Size Effect for Specific Energy in Grinding of Silicon Nitride. *Wear* , 862-867.

29] Chandrasekar, S., & Sathyanarayanan, G. (1987). *15th North American Manufacturing Research Proceedings v.2,* (pp. 499-505). Manufacturing Technology Review.

30] http://optics.nasa.gov/tech_days/tech_days_2003/docs/39TrexCVCSiC.pdf

31] Nettleship, I., & Stevens, R. (1987). Tetragonal Zirconia Polycrystal (TZP)- A Review. *International Journal of High Technology Ceramics 3* , 1-32.

32] http://coorstek.com/materials/ceramics/alumina/ad995.asp

33] LA-700 Specification Sheet, Horiba 1998

34] Wang, H., Lin, H. T., Wereszczak, A. A., Yang, N. and Jensen, J. A., Specific energy and scratch hardness of gamma titanium aluminides subjected to single-grit pendulum scratching, Proceedings of ASME/ICEF 2006, Paper No. ICEF2006-1532.

35] Koepke, B., & Stokes, R. (1970). A Study of Grinding Damage in Magnesium Oxide Single Crystals. *Journal of Materials Science* , 24-247.

36] Lowrison, G. C. (1974). *Crushing and Grinding: The Size Reduction of Solid Materials.* London: Butterworths. P.67

37] Lankford, J., & Blanchard, C. (1991). Fragmenation of brittle materails at high rates of loading. *Journal of Materials Science 26* , 3067-3072.

38] M.V. Swain and R.H.J. Hannink, Metastability of the martensitic transformation in a 12 mol% ceria-zirconia alloy: grinding studies, *Journal of the American Ceramic Society* **72** (1989), pp. 1358–1364.